https://dx.doi.org/10.1016/j.engstruct.2022.114107

Study on stainless steel blind bolted T-stub to concrete-filled stainless steel tube connections

Ying-Lei Li [a] and Xiao-Ling Zhao [a,b,*]

[a] School of Civil and Environmental Engineering, UNSW Sydney, Kensington, NSW, Australia

[b] Department of Civil and Environmental Engineering, The Hong Kong Polytechnic University, Hong Kong, China

(* corresponding author: xiaolin.zhao@unsw.edu.au)

Abstract:

Tension zone of a bolted steel beam-to-column connection can be represented by an equivalent T-stub to column connection under tensile load as recommended in Eurocode 3. This paper presents an experimental and theoretical study on equivalent T-stub to concrete filled stainless steel tube connections (T-to-CFSST) and the basic component (CFSSTs). Both stainless steel blind bolts and normal bolts were selected for the connections. Effects of various parameters, including tube thickness, bolt layout, bolt size, bolt type and bolting method, on the performance of T-to-CFSST and CFSST were investigated. Compared to hollow tubes, filling concrete could greatly enhance the stiffness and strength of the connections. Anchorage between bolts and concrete could be improved by setting studs at bolt ends. A finite element (FE) model was developed in this study and its accuracy was validated by the experimental results. Parametrical study was conducted to investigate the effects of parameters that cannot be covered in experiments, such as material type, tube length and T-stub thickness, on the behavior of CFSST and T-to-CFSST. Based on the experimental and numerical results, theoretical models were proposed to estimate the load-displacement curves of CFSSTs and their stiffness, yield capacity and ultimate capacity. By adopting the concept of component method,

formulas were also proposed to predict the stiffness, yield capacity and ultimate capacity of T-to-CFSSTs. In general, the prediction matched well with the experimental results of CFSSTs and T-to-CFSSTs.

Keyword: Stainless steel blind bolt; concrete-filled stainless steel tubes (CFSST); T-to-CFSST connections; seawater and sea sand concrete

1. Introduction

Blind bolting system only requires one side access of the connected sections and is increasingly used in open-to-closed section connections [1]. Commercially available blind bolts include the Hollo-bolt [2], the Flowdrill [3], the Ajax Oneside bolt [4], the Ultra-Twist blind bolt [5], the Blind bolt [6], the TW bolt [6] and the heavy duty bolt [6]. Owing to the flexibility of hollow section face, it is difficult to develop a rigid connection [7]. By filling concrete into the hollow section, the strength and stiffness of a connection could be significantly enhanced [8, 9]. In coastal areas that are lack in fresh water and river sand, seawater and sea sand concrete (SWSSC) is an alternative construction material. Due to the Chloride ions in seawater and sea sand, corrosion resistant materials, such as fiber reinforced polymer (FRP) and stainless steel (SS), are suggested to reinforce SWSSC [e.g. 10, 11].

Although studies on stainless steel blind bolted connections are rather rare, extensive research has been conducted on carbon steel blind bolted connections. France et al. [8] found a dramatic increase in strength and stiffness of concrete-filled flowdrill joints when compared with their unfilled equivalent. However, ductility of the joint is significant less for concrete-filled tubes. Wang et al. [12] compared the cyclic behavior of blind bolted beam-to-column joints with different stiffening elements including binding bars, internal rings, external C-shaped channels and internal I-sections and concluded that C-shaped channels and I-sections could significantly improve the performance of the joints. A series of experimental investigations was conducted in [13-16] for blind bolt I-beam to

concrete-filled tube joints, which covered extended and flush end plate joints, monotonic and seismic behaviors, fully filled and double-skin tubular columns and joints with or without slabs. Agheshlui et al. [17] studied the behavior of anchored blind bolted composite connection to a concrete filled steel tubular column and proposed a simplified model for the connection. Tao et al. [18] experimentally investigated the behavior of blind bolted connections to concrete-filled stainless steel columns. It was found that the presence of composite slabs, setting binding bars and using circular column (comparing to square column) could significantly improve the performance of joints in terms of initial stiffness and strength.

In order to further increase the stiffness in blind bolted joints, scholars proposed various methods to improve the anchorage of blind bolts in concrete, such as welding extensions [19] and studs [20]. Tensile behavior of single anchored blind bolt in concrete-filled steel tubes was studied to understand the interactive effect between the bolt, concrete and tube [21, 22]. Behavior of a group of blind bolts was investigated by conducting tensile test on T-stub to concrete-filled tubes [23, 24]. Effects of bolt gauge, bolt pitch, tube thickness, concrete strength and tube shape on their performance were extensively studied [25-27]. Besides blind bolting technology, researchers proposed to use through bolts for connection between I-beam and concrete-filled steel tubular columns [28, 29]. The concrete core works together with the column face to support the tension force in the bolts so that the stiffness and resistance could be improved.

Currently, the standards (e.g., EN1993-1-8 [30]) have not offered a design method for blind bolted connections to concrete-filled steel tubes. Due to the presence of infill concrete, the compression side of the column will act as a stiff part. At the tension side, the face wall may be considered as a clamped plate at the junction with column side walls [31]. Silva et al. [32] proposed an analytical model based on an equivalent strip of the loaded column face to predict the stiffness of joints to concrete filled

rectangular tubes. Elamin [33] proposed an analytic model to predict the load-displacement curve by firstly determining the key parameters of initial stiffness, yield resistance and post-yield stiffness. Based on FEM results, Thai and Uy [34] proposed methods to estimate the rotational stiffness and moment resistance of bolted endplate joints with hollow or CFST columns. Currently, it is still lack of reasonable design method to predict the initial stiffness and capacities of concrete-filled stainless steel tubes and beam-to-column connections made by stainless steel.

In general, the research on blind bolted connections to concrete-filled tubes is still limited and it is lack of appropriate design methods. No study has been reported for stainless steel blind bolted joints, which are preferred to be used in corrosive environments (e.g., seawater and sea sand concrete [35]). This paper presents an experimental and analytical study on stainless steel blind bolted T-stub to concrete-filled square stainless steel tubes (CFSST) connections subjected to tensile loads. Both the structural behavior of CFSSTs and T-to-CFSST joints were investigated. In order to evaluate the effects of parameters, which were not covered in experiments, on the structural behavior of CFSSTs and T-to-CFSSTs, FE models were developed and parametrical study was conducted. Finally, theoretical models were proposed to estimate the load-displacement response, resistance and stiffness of them. This paper is a follow-up of the authors' previous paper [36] that focused on T-to-hollow tube connections. Effect of infilled concrete on the structural behavior was also discussed in the current paper.

2. Experiment program

Four types of specimen configurations were adopted to study the behavior of concrete-filled stainless steel tubes (I and II in Fig. 1) and T-stub to CFSST connections (III and IV in Fig. 1) under axial tension. T-stub was formed by TIG welding two stainless steel plates and the welds have a comparable strength to the raw materials. Stainless steel square tube was manufactured by cold-forming and a

welding seam was located at the middle of a side wall. The grade for stainless steel in T-stubs and tubes is 304. Three types of SS blind bolt (A, B and C), SS normal bolt (D), SS through bolt (E, as shown in IV of Fig. 1) and SS normal bolt with anchor (F, as shown in II in Fig. 1) were used in this study. Details of the blind bolts and their mechanical properties can be found in the authors' previous paper [36] and the photos of blind bolts will be shown in Fig.7 . In type E and F bolts, the bolt shank was replaced by a stainless steel threaded rod. For type F bolt, the length of the rod imbedded in concrete is 50 mm and a M16 hexagon nut (thickness of 12 mm) is fixed at the end as the anchor.

A total of nineteen specimens were tested in this study and specimen details are listed in Table 1, where the definitions of W, L, t_{tube} and t_T are illustrated in Fig. 2. Length of the SS tube is 200 mm and its width is 150 mm. Dimension of the flange of T-stub is 150 mm by 150 mm. For an ease installation of a group of bolts, diameter of the bolt hole is 0.5 mm larger than the nominal diameter of a bolt. Label of the specimen is defined as: "F" (indicating filled with concrete)-"t" (indicating tube) followed by its nominal thickness-"T" (indicating T-stub) followed by its nominal thickness-"W×L"(layout of bolt)-"M" followed by bolt size and type.

Fig. 3 shows the CFSST and T-to-CFSST connection specimens before casting concrete. For CFSST specimens, 15 mm thick timber plates were used for positioning the bolts. After the concrete is hardened, the timber plates were removed. The nuts in T-to-CFSST specimens were snug tightened before casting concrete and the pretention force in bolts is assumed to be negligible. Seawater sea sand concrete (SWSSC) was casted for all the specimens. The mixture is: general purpose cement (180 kg/m^3), granulated blast furnace slag (180 kg/m^3), seawater (190 kg/m^3), sea sand (800 kg/m^3) and coarse aggregate (~10 mm, 1050 kg/m^3). Two batched of concrete were casted and three concrete cylinders (diameter of 100 mm and height of 200 mm) were prepared for each batch to measure the

compressive strength. Axial compression test was conducted on the cylinders and the average compressive strength is 49.0 MPa at the test date (±2 days) of specimens.

Experimental setup for the tensile test of CFSSTs and T-to-CFSSTs is shown in Fig. 4 (a) and (b), respectively. As shown in Fig. 4 (a), CFSST is bolt connected to the 40 mm thick rigid end plate rig, which is gripped by a 1000 kN testing machine. During the experiment, the end plate was in elastic and its deformation was negligible. The vertical displacement was recorded by the test machine and the relative displacement between the tube side walls was monitored by a draw wire sensor located at the mid-height of the tube. Two strain gauges were installed at the middle of the side walls to measure the vertical strain of the tube surface. Experiment for T-to-tube connections was conducted in a 250 kN universal test machine (Fig. 4 (b)). Webs of T-stubs were gripped by the machine. Layout of the strain gauges and draw wire sensor was same as that for CFSSTs. All the experiments were running in displacement control and the loading speed is 2 mm/min.

3. Experimental results

3.1 CFSST

Material properties of stainless steel tube have been measured by tensile coupon test and reported in [36]. The yield stress (f_y, 0.2% proof stress) for SS tube with nominal thickness of 3 mm and 6 mm is 379.0 MPa and 443.9 MPa, respectively, whereas the ultimate stress is 751.5 MPa and 755.3 MPa, respectively [36]. The stress-strain curve of stainless steel exhibits a round shape with substantial strain hardening.

Failure modes of CFSSTs under tensile load are presented in Fig. 5, corresponding to the end of the loading process. The inward deflection of the tube side walls was resisted by the concrete, leading to a negligible deflection of the side walls. For specimens with bolt type D, the tube face walls were

separated from the concrete and most of the displacement was contributed by the deflection of face walls. Furthermore, the concrete in the corners were crushed due to the compressive force from the tube. Punching shear failure (i.e., pull out of bolts) occurred for specimens with $W \times L$ of 50×100 and 100×100, whereas fracture of tube at the face-to-side wall junction happened for specimens if $W \times L$ is 100×50. In specimens with bolt type F, anchorage failure in concrete occurred first leading to a considerable drop of the applied load. Thereafter, the force was fully transferred to tube face walls. The load was resisted by the tube in a similar way as specimens with bolt type D until the fracture of tube occurred.

Load-displacement curves of CFSSTs are plotted in Fig. 6, where the displacement is the relative movement between the rigid end plates. CFSSTs with bolt type D generally exhibit a bilinear shape of load-displacement curve, which is in a similar pattern as hollow tubes [36]. For a design purpose, the yield capacity ($N_{y,t}$) is defined as the load at which the curve starts to deviate from its initial linear region and the corresponding displacement is $\Delta_{y,t}$. The ultimate capacity ($N_{u,t}$) is defined as the load at $\Delta_{u,t}$ that is three times of $\Delta_{y,t}$. These definitions are same as those in [36], which are based on past researches on tubular structures [37-40]. However, if the bolts were imbedded in concrete (i.e., bolt type F), anchorage failure occurred at the early stage of the loading process leading to a considerable drop of the applied load. Thereafter, the load kept consistent with some fluctuation along the increase in displacement until the fracture of tube. For these specimens (i.e., F-t3-50x100-M16F and F-t3-100x50-M16F), only the ultimate capacity was defined as the first peak load, which is the load corresponding to the anchorage failure. By comparing Fig. 5 and Fig. 6, it is found that a dramatic drop of load occurs in CFSSTs which is caused by an abrupt fracture failure of tube. Nevertheless, the load drops gradually if the punching shear failure occurs. Key experimental results of CFSSTs under tension are summarized in Table 2, where $K_{i,t}$ is the initial stiffness defined as the slope of the initial part of the load-displacement curves.

3.2 T-to-CFSST

Failure modes of T-to-CFSST connections are presented in Fig. 7, in which the photos for each bolt type are also given. Because the T-stub is only 6 mm thick, large deformation of T-stubs could be observed. Depending on the bolt type and size, either fracture of bolt or pull out of bolt (i.e., punching shear failure) occurred in the connections. Pullout of bolts occurred in specimen F-t3-T6-100x100-M12B and bolt fracture failure occurred in all the other specimens. During the late stage of the loading process, the bolts were severely bent due to the large deformation of the flange of T-stubs. Except connections with through rods (type E), the deformed shape of CFSSTs was similar as that shown in Section 3.1, in which the tube face walls were pulled upward/downward and the displacement of tube side walls was insignificant. As the failure load of T-to-CFSST connections is lower than that of CFSSTs in Section 3.1, the deformation of tube face walls in T-to-CFSST connections is less than that in CFSSTs.

Load-displacement curves of T-to-CFSST connections are shown in Fig. 8, where the displacement is based on the position reading of the testing machine (i.e., relative movement of the top and bottom grips). Owing to the limited capacity of the test machine, test for specimen F-t6-T6-100x100-M16D and F-t6-T6-100x100-M16E was terminated before reaching their ultimate state. In this study, connections with blind bolts exhibited lower capacity than connections with normal bolts. It is mainly caused by that the net area in blind bolts to resist the applied force is smaller than the net area of normal bolts. An abrupt drop of the applied load was observed for all specimens at failure (either bolt fracture or pullout of bolt). As shown in Fig. 8, the load-displacement curves are generally in bilinear shape. The displacement consisted of the deformation of CFSST, T-stubs and bolts, among which T-stubs contribute a major part of the displacement.

Due to the difficulty of finding the yield point and ultimate point directly from the load-displacement curves of T-to-CFSST connections, the yield and ultimate displacements are defined from CFSSTs and T-stubs. It is assumed that the yield displacement ($\Delta_{y,t}$) is equal to the summation of $\Delta_{y,t}$ of CFSSTs defined in Section 3.1 and two times of $\Delta_{y,t}$ of T-stubs defined in Li and Zhao [36]. The ultimate displacement ($\Delta_{u,t}$) for T-to-CFSST connections is defined in a similar way. $\Delta_{y,t}$ and $\Delta_{u,t}$ of T-stubs measured in [36] were 1.25 mm and 5.0 mm, respectively. After knowing $\Delta_{y,t}$ and $\Delta_{u,t}$, the corresponding experimental yield capacity ($N_{y,t)}$ and ultimate capacity ($N_{u,t}$) can be read from the load-displacement curves. Table 3 summarizes the key test results of T-to-CFSST connections.

4. Discussions

4.1 CFSST

4.1.1 Effects of bolt layout and tube thickness

As the face wall of CFSST behaves similarly as a plate (two sides are fixed and the other two sides are free), the bolt distance along the direction perpendicular to the tube axis (W) could greatly affect the behavior of CFSST. By increasing W from 50 mm to 100 mm (L=100 mm), the capacity ($N_{y,t}$ and $N_{u,t}$) increased by 83%~162%, and the initial stiffness increased by 218%~313%. The influence of the bolt distance along the tube axis (L) is insignificant: the capacity ratio of CFSST with L=100 mm to L=50 mm (W=100 mm) varied from 0.79 to 1.17 and the initial stiffness ratio varied from 0.74 to 0.92. The decrease in initial stiffness is caused by the fact that if the forces are located near the free edges (i.e., L=100 mm), the face wall could deform more than the case of forces located away from the edges (i.e., L=50 mm). When bolt layout (W×L) changed from 100×100 to 100×50, the failure mode also changed from pull out of bolts to fracture of tube. The reason is that if L=100 mm, the stress in the tube face-to-side wall junction is more uniform than the case of L=50 mm. As expected, the thickness of SS tube has a substantial effect on the behavior of CFSSTs. The capacity ratio of CFSSTs with t_{tube}=2.63 mm to t_{tube}=5.38 mm varied from 3.50 to 5.00, whereas the initial stiffness

ratio of them is 2.75~4.46. In general, increasing tube thickness and locating bolts near the side walls are the effective methods to improve the capacity and initial stiffness of CFSSTs.

4.1.2 Effect of anchorage

A comparison of load-displacement curves of CFSSTs with (bolt type F) and without anchorage (bolt type D) is shown in Fig. 9 (a). The initial stiffness ratio of CFSSTs with anchorage to CFSSTs without anchorage is 19.2 for bolt layout of 50×100 whereas the ratio is 4.0 for bolt layout of 100×50. If setting anchorage, the effect of *W* on the initial stiffness becomes insignificant (i.e., 120.7 kN/mm for F-t3-50x100-M16F and 139.3 kN/mm for F-t3-100x50-M16F) as the initial stiffness is mainly contributed by the concrete instead of the bending stiffness of tube face walls. As shown in Fig. 9 (a), the displacement corresponding to the ultimate capacity of CFSSTs with anchorage is much less than that without anchorage. Anchorage failure occurred very early owing to the brittle feature of concrete. Fig. 9 (b) shows the load-strain curves of CFSSTs, where the strain is the average reading of strain gauges vertically fixed in the middle of side walls. The strain almost keeps zero for CFSSTs with anchorage until reaching about 40 kN. Within this stage, the stress in tube side walls is negligible indicating that the applied force is mainly transferred by concrete. For specimen F-t3-50x100-M16F, there is a slight drop of the applied load and a fast increase of strain at about 40 kN that is probably caused by the debonding between concrete and tube face walls. During the whole loading process, the strain was less than the yield strain of stainless steel (i.e., 3817 με [36]) indicating the side walls were not yielded.

For CFSSTs with and without anchorage, the stress transfer mechanisms are different (Fig. 10 (a)). If the bolt is not imbedded in concrete (i.e. bolt type D), the applied force is mainly resisted by the tube face wall in bending. On the other hand, if the bolt is anchored in concrete, both tube face wall and concrete could resist the load together. The stress concentration near the bolt hole is also mitigated.

By comparing the load-displacement curves of specimen F-t3-100x50-M16D and F-t3-100x50-M16F, it is found that CFSST with anchorage has a much higher ultimate capacity. This is mainly attributed to the fact that the stress is more widely distributed in tube side walls and concrete if having anchorage (Fig. 10 (b)). This explanation is also verified by the experimental observation that the strain in CFSSTs with anchorage is lower.

4.1.3 Effect of concrete infill

By filling concrete, the structural behavior of stainless steel tubes greatly changed. Fig. 11 shows the deformed shapes of the face walls of some CFSSTs and their counterpart hollow sections [36] after test. For hollow sections, the face wall behaves like a flat beam and yield lines are formed at bolt lines. However, the face wall in CFSSTs behaves like a plate with two sides are fixed and the other two sides are free. Yield lines are formed around bolt holes and the out of plane deformation of face walls varies along the tube axis. It is clear that the concrete infill changes the yield line pattern of tubes at ultimate state. It is necessary to mention that during the early loading process, the deformed shapes of CFSSTs with or without concrete were generally similar.

A comparison of load-displacement curves between CFSSTs and hollow sections is shown in Fig. 12, where the solid line indicates CFSSTs and the dashed line represents corresponding hollow sections [36]. By filling concrete, the bilinear shape of the curves does not change. However, the initial stiffness and load-carrying capacity are significantly enhanced. The displacement corresponding to the peak load (i.e., specimen failure) of CFSSTs is larger than that of hollow sections, indicating a lower ability of CFSSTs to deform. This is because the inward deformation of tube side walls is restrained by the concrete. The enhancement ratio by filling concrete, which is the ratio of peak load or initial stiffness of CFSSTs to that of hollow sections, is also given in Fig. 12. The enhancement ratio for peak load ranges from 1.10 to 3.95, whereas the ratio for initial stiffness is 2.68~6.56. The

beneficial effect of filling concrete is more pronounced for improving stiffness than capacity. If filled with concrete, the initial stiffness of CFSSTs is improved by three ways: (1) restraining the inward bending deformation of side walls; (2) changing the boundary condition of face walls from semi-fixed (i.e., pined with somewhat rotation restraint) to almost fixed; and (3) providing anchorage.

Comparison of load-strain curves of CFSSTs and hollow sections is shown in Fig. 13, where the deformed shape is illustrated in dashed lines. In CFSSTs, the side wall is in tension (i.e., positive strain reading). In hollow sections, the strain is negative (i.e., outer surface of side wall is in compression) indicating the compressive strain caused by bending is overwhelming than the tensile strain induced by the applied load. As shown in Fig. 13, effect of W on the strain is more significant for hollow sections than that of CFSSTs as the bending deformation of side walls is negligible if filled with concrete.

4.2 T-to-CFSST

4.2.1 Effect of bolt type, bolt size and tube thickness

T-to-CFSST connection is consisted of T-stub and CFSST, both of which would affect the behavior of the connection. Variables investigated in this study for T-to-CFSST connections include bolt type, bolt size and tube thickness. Other parameters, including bolt layout (W×L) and T-stub dimensions, are the same for all specimens. In general, all connections exhibit a bi-linear feature of the load-displacement curves (Fig. 8). The initial stiffness of connections with blind bolts is larger than that of connections with normal bolts (Table 3). As part of the blind bolt, such as the sprayed legs and bolt shank, is embedded in concrete, the infilled concrete could also contribute to the initial stiffness. Connections with normal bolts generally have a higher peak load than connections with blind bolts. In order to achieve the one-side access during installation, special interlocking mechanism is adopted for blind bolts, which reduces the net cross-section area to resist the load. Fracture of blind bolts occur in the weakest parts along the bolt shank, whose cross-section area is smaller than the nominal area

calculated from the nominal diameter. Due to the different interlocking mechanisms, the behavior of connections with different blind bolt types is also different. It seems that connections with blind bolt type A have the best anchorage to concrete, as demonstrated by a higher initial stiffness of them. As expected, with the increase in bolt size and tube thickness, both the initial stiffness and load-carrying capacity increases (Table 3).

4.2.2 Effect of concrete infill

By filling concrete, the failure mode of T-to-CFSST connections with blind bolts is changed. Fracture of blind bolts (except M12B) was observed in T-to-CFSST connections. However, in tests for T-to-SHS connections and single bolts, the failure mode is sever bending of bolt shank (type A), pull out of bolts (type B), cutting off of bolt legs (type C) [36]. It is clear that the strength of blind bolt is fully utilized in T-to-CFSST connections as anchorage is formed between blind bolt and concrete. Blind bolt would have an equivalent strength to the normal bolt with the same net cross-section area.

A comparison of the load-displacement curves between T-to-CFSST connections and T-to-SHS connections is shown in Fig. 14. The shape of the curves does not change significantly if filled with concrete. It should be noted that the deformation of T-stubs contribute to a major part of the total displacement and the sizes of T-stubs are the same for both connections. Enhancement ratio by filling concrete in terms of initial stiffness and peak load is also given in Fig. 14, in which the peak load is defined in Fig. 14. The beneficial effect of enhancing the load-carrying capacity by filling concrete for T-to-CFSST connections is not as significant as that for CFSSTs (Section 4.1.3). For connections with blind bolts, as the bolts could be anchored in concrete to avoid being pulled out from holes, filling concrete could substantially increase the initial stiffness. Nevertheless, the enhancement effect is less significant for connections with normal bolts as the concrete does not directly contribute to the initial stiffness by anchorage effect.

4.2.3 Effect of specimen configuration

Besides blind bolt, through bolt is another option as fasteners to connect closed sections. Fig. 15 (a) shows the load-displacement curves of T-to-CFSST connections with one-side bolts (configuration III in Fig. 1) and through bolts (configuration IV in Fig. 1). Specimens with through bolts have a higher stiffness and load-carrying capacity. In this configuration, the applied load could be directly transferred within the through bolts and bending deformation of tube face walls is reduced due to the change of load transfer mechanism. Load-strain curves of the connections are plotted in Fig. 15 (b), where the strain gauges were attached in the middle of tube side walls. For specimens with one-side bolt (type D), tensile strain is observed, and the values are less than the yield strain. However, the strain in the side walls of specimens with through bolts is negligible (i.e., less than 50 με) and compressive strain is even observed for specimen F-t3-T6-100x100-M16E. The very small value of strain indicates that the stress in tube side walls is negligible, which is probably caused by two reasons: (1) most of the load is directly transferred by the through bolts; (2) due to the prying force, the tube side walls are probably in compression. Nevertheless, it is found that the prying effect in CFSSTs is much less significant than that in hollow section by examining the deformed shapes of them.

5. FE analysis

5.1 FE model

Finite element (FE) analysis is conducted in ABAQUS/Explicit module [41]. Comparing to implicit solver in Standard module, explicit solver is more suitable for the analysis involving complex contact and nonlinear problems to avoid numerical convergence difficulties. In this study, both material and geometric nonlinearities are accounted in the FE analysis. Due to the symmetry of specimen geometry and loads, only 1/8 of a specimen is modelled to save computation time.

The classical metal plasticity model implementing Mises yield surface, isotropic hardening and associated plastic flow rule is adopted for steel components (i.e., tube, T-stub and bolt). As the yield stress of steel is orders of magnitude less than the elastic modulus, the experimental stress-strain data should be converted to the "true" stress-strain data for ABAQUS input [42]. In this study, *E* for stainless steel is taken as 195 GPa and Poisson's ratio is 0.3. Owing to cold-forming effect, the stress-strain relationship of corners in a square stainless steel tube is different from that of the flat regions. The formulas proposed in [43] are adopted to estimate the stress-strain response of the corner material affected by cold-forming effect. Details of these formulas could be found in Li and Zhao [44] and Wang et al. [43]. Fig. 16 plots the "true" stress-strain relationship of stainless steel tubes and T-stubs used for FE analysis. Ramberg-Osgood model [45] is adopted for stainless steel bolts due to the difficulty in measuring the full range stress-strain curve in single bolt tests. In Ramberg-Osgood model, the stress-strain relationship is derived from yield stress, initial elastic modulus (=195 GPa) and a constant (=7.5), among which the yield stress is obtained from the single bolt test [36]. In the FE model for CFSST test, the mild steel end plate is modeled as an elastic material with Young's modulus of 206 GPa and Poisson's ratio of 0.3.

For concrete material, its Young's modulus is determined as $4730\sqrt{f_c'}$ (in MPa) and Poisson's ratio is set as 0.2. The linear Drucker-Prager (D-P) model in ABAQUS is adopted to simulate the concrete plasticity [42]. By assuming the triaxial compressive strength is 3.5 times of the uniaxial compressive strength [46], the friction angle is derived as 53.7°. In ABAQUS, the stress flow ratio is used to define the shape of yield surface in deviatoric plane and it is set as 0.78 in this study. In a D-P model, the hardening rule can be defined by using a single uniaxial stress-strain curve of concrete. In this study, the stress-strain relationship is obtained by Carreira and Chun's [47] model, in which the concrete ultimate strain is taken as $0.000937\sqrt[4]{f_c'}$ [48] (f_c' in MPa). A constant dilation angle that ranges from

20° to 40° was commonly adopted by researchers [49, 50] to represent the flow rule of concrete and 30° is adopted for this study. It is necessary to mention that in a T-to-CFSST connection, the infilled concrete mainly acts as a solid component to resist the deformation of the stainless steel tube and the behavior of the T-to-CFSST connection is not sensitive to these parameters for the linear D-P model. All the other parameters not specified in this paper are set as default in ABAQUS.

The stainless steel tube, concrete, T-stub, end plate and bolts are modeled by the 8-node 3-D solid element with reduced integration (C3D8R). Welding in T-stub was not modelled as it has equal strength to the raw material and no failure occurred in weldings. A structured meshing technique is adopted to achieve hexahedral element shape. The meshes around holes and corners are refined and at least three layers of elements are generated along the thickness direction of tubes and T-stubs to guarantee the analysis accuracy. The FE model for CFSST and T-to-CFSST is illustrated in Fig. 17.

A “surface-to-surface” contact interaction is developed for the FE models to avoid the penetration of components. The friction coefficient is set as 0.1 and the normal behavior is set as “hard” contact. The contacted surfaces involved in the model include tube-to-concrete/T-stub/end plate and bolt-to-concrete/tube/T-stub/end plate.

Since 1/8 specimen is modeled in this study, additional boundary conditions are added to the symmetric planes. Displacements in X-direction, Y-direction and Z-direction at the left, bottom and front planes are constrained, respectively. For an easy convergence of the solution, upward displacement is applied on the top surface of end plate (for CFSST) or the top surface of T-stub (For T-to-CFSST). The displacement is applied with a smooth step amplitude curve to avoid generating waves due to discontinuity in the rate of applied loading. During the analysis, the kinetic energy of

the deforming material does not exceed 1% of its internal energy, which meets the requirement for quasi-static analysis with ABAQUS/Explicit.

5.2 Verification of FE model

Four specimens (i.e., F-t6-50x100-M16D, F-t6-100x50-M16D, F-t6-100x100-M16D and F-t6-T6-50x100-M16D in Table 1) are selected to verify the FE models. In FE analysis, fracture of bolts and tubes cannot be simulated. The analysis is terminated when the Mises stress in tubes or bolts reaches the ultimate stress, indicating the fracture of steel material. A comparison of the experimental and FE analyzed load-displacement curves of CFFSTs and T-to-CFSST connection is shown in Fig. 18, which are in good agreement. Fig. 19 shows the failure modes and Mises stress contour of these selected specimen. Stress concentration occurs around bolt holes and high stress is observed at tube's flange-to-web junction, indicating these areas are prone to fracture. Most of the deformation occurs in stainless steel tubes and T-stubs and the separation between concrete and tube is observed in FE results. In general, the simulated failure mode agrees well with the experimental observations in Figs. 5 and 7. Therefore, the FE models developed in this study is accurate and can be used for the parametrical studies.

5.3 Parametrical study for CFSST

5.3.1 Effect of material type

It is known that stainless steel has a round shape stress-strain relationship without yield point. Fig. 20 shows the load-displacement curves of CFSST with three material models incorporating different strain hardening rules for the tube. The Ramberg-Osgood model is for stainless steel and the other two models (i.e., elastic-linear hardening and elastic-perfect plastic) can be used for mild steel. The Yield stress and ultimate stress are set as 400 MPa and 800 MPa, respectively. It is evident that the material type has a significant effect on the load-displacement curves of CFSSTs as the load capacity

is controlled by material strength instead of stability. It can be expected that stainless steel tube-to-beam connection has a higher load-carrying capacity than carbon steel tube-to-beam connection. Nevertheless, the effect of material type on the initial stiffness is negligible owing to a similar Young's modulus of stainless steel and carbon steel.

5.3.2 Effect of tube length

In the current experimental study, the length of CFSSTs is 200 mm due to the limitation of experimental facilities. However, in a column-to-beam connection, the length of column taking part in resisting the applied load (in the form of equivalent tensile force) maybe larger than 200 mm. It is necessary to investigate the effect of CFSST length (l_{CFSST}) on the load-displacement curves.

Fig. 21 shows the load-displacement curves of CFSSTs with various lengths (i.e., l_{CFSST}=200, 400 or 600 mm). By increasing l_{CFSST} from 200 mm to 400 mm, the applied load increases by 0~15% depending on the displacement levels. At the ultimate displacement limit ($\Delta_{u,t}$) given in Table 2, the increase in load is less than 9%. However, effect of l_{CFSST} on load-displacement curves is negligible if CFSST is longer than 400 mm. It seems that the effective length of CFSSTs in this study that participates in resisting the applied load is around 400 mm. It should keep in mind that the effective length depends on various parameters, such as the dimensions of CFSSTs (e.g., width, thickness), layout of bolts (W and L) and the material properties.

The deformed shape and Mises stress contour of CFSSTs with various lengths are shown in Fig. 22. The upward deformation of CFSST face walls becomes less obvious when they are near the ends, confirming that there exists an effective length for CFSST to resist the applied load. Consequently, the stress near CFSST ends is small. The distribution of stress in the middle plane of tube side wall, which is the reaction stress in FE models, is plotted in Fig. 22 as well. Summation of the stress is

equal to the applied load. In CFSSTs with 200 mm length the reaction stress variation is insignificant but for CFSSTs longer than 400 mm, the reaction stress near ends is almost zero, which agrees with the stress contour. However, it is found that although the load-displacement curves are identical for CFSSTs with 400 mm and 600 mm length, the distributions of reaction stress are different.

5.4 Parametrical study for T-to-CFSST

5.4.1 Effect of material type and tube length

Effects of material type and CFSST length on the load-displacement curves have been discussed in Section 5.3. Those conclusions for CFSSTs can be also applied to T-to-CFSST connections since CFSST is the basic component for T-to-CFSST connections.

5.4.2 Effect of T-stub thickness, bolt size and bolt layout

Deformed shape and Mises stress contour of specimens with various t_T, bolt size and bolt layout (L) are shown in Fig. 23. The benchmark specimen is label as "F-t6-T9-100x100-M16D" whose tube thickness is 6 mm, t_T (T-stub thickness) is 9 mm, bolt size is M16D and L (bolts layout) is 100 mm. The load-displacement curves of these specimens are plotted in Fig. 24. With the increase in T-stub thickness, the load capacity increases obviously. As shown in Fig. 23, a thicker T-stub has less plastic deformation in flanges due to a higher bending stiffness. However, the large deformation in bolts, which is caused by the high load capacity of the specimen leads to a reduction of the clamping effect on T-stubs resulting in a large rotation of the T-stub flange. Bolt size also has a significant effect on the behavior of T-to-CFSST connections by comparing the specimens with bolt size of M12D, M16D and M20D. If the bolt diameter is too small (e.g., M12D), strength of bolt may control the capacity of the connection and large deformation occurs in bolts resulting in a reduction of the clamping effect. As shown in Figs. 23 and 24 (L=50 vs 100 vs 120 mm), layout of bolt (L) could greatly affect the behavior of T-to-CFSST connections as the force arm in T-stub is changed. In a T-to-CFSST

connection, most of the deformation is contributed by the deformations of T-stub flange and bolts. Furthermore, the deformation in T-stub flange is controlled by the bending and rotation of the flange. If the T-stub is thick and bolt diameter is small (i.e., low clapping effect), rotation of the flange would be the major source of the deformation, otherwise bending is the major source. In order to fully utilize the strength of each component in a T-to-CFSST connection, contribution of each component should be comparable.

It is known that prying force may exist in T-stubs, in which the force in bolt (N_{bolt} in Fig. 25) is larger than the load applied on the T-stub (N in Fig. 25). Fig. 25 plots the N_{bolt}-displacement curves and N_{bolt}/N-displacement curves to evaluate the prying effect in a T-to-CFSST connection. A higher value of N_{bolt}/N means a severe prying effect for T-stub. With the increase in displacement, load in bolt increases. Except the specimen with t_T=6 mm, M16 bolt and L=100 or 120 mm, N_{bolt}/N keeps constant during the loading process. As shown in Fig. 25, the prying effect can be mitigated by increasing t_T, increasing bolt diameter or reducing L. As prying force leads to overloading of the bolts in tension, prying effect may need to be accounted when estimating the capacity of T-stub. Nevertheless, capacity estimation for T-stub exceeds the scope of the current study.

6. Theoretical analysis

6.1 CFSST

6.1.1 Initial stiffness

CFSSTs under tensile loads could be simplified as a 2-D model (Fig. 26 (a)) by assuming the stress is uniform along the tube axis (within the effective tube length, l_{eff}) at yield capacity. For specimens tested in this study, as the tube length is short (i.e, l_{tube}=200 mm) and tube deformation is uniform (Fig. 22), l_{eff} is set as the tube length (l_{tube}). If the tube length is larger than 200 mm, a factor may need to be implemented to estimate the effective length. Based on experimental observation, inward

deformation of the side walls was restrained by concrete and the side walls were in tension. The tube face wall behaves like a beam with fixed end supports (Fig. 26 (b)). As the face wall is tightly connected to the end plates, the deformation of face walls underneath the end plates could not deform towards the end plates. Therefore, the middle part of the beam (highlighted in thick line in Fig. 26 (b), *W*) could be regarded as rigid.

Initial stiffness of CFSST is defined as the slope of the initial part (i.e., elastic region) of the load-displacement curve and the predicted initial stiffness could be calculated by Eq. (1).

$$K_{\mathrm{i,p}}^{\mathrm{CFSST}} = \frac{2F}{2\Delta} = \frac{F}{\Delta} \tag{1}$$

where *F* is the applied force and *Δ* is the corresponding displacement (Fig. 26 (b)). Based on structural mechanics, as the tube face wall is in elastic, the deflection could be determined by Eq. (2). Substituting Eq. (2) into Eq. (1), the predicted initial stiffness could be calculated by Eq. (3):

$$\Delta = \frac{F(b_{\mathrm{tube}} - t_{\mathrm{tube}} - W)^3}{96EI} \tag{2}$$

$$K_{\mathrm{i,p}}^{\mathrm{CFSST}} = \frac{96EI}{(b_{\mathrm{tube}} - t_{\mathrm{tube}} - W)^3} \tag{3}$$

where b_{tube} is width of SS tube, t_{tube} is thickness of SS tube, *W* is bolt distance, *E* is Young's modulus of SS setting as 195 GPa, *I* is the second moment of initial of tube face wall that is equal to $\frac{1}{12} l_{\mathrm{eff}} t_{\mathrm{tube}}^3$, where l_{eff} is taken as tube length (l_{tube}) in this study. It is necessary to mention that if the tube length is larger than 200 mm, the effective length of tube should be properly determined based on further research on the effect of tube length on the connection behavior.

In the CFSST experiment, the measured initial stiffness ($K_{i,t}$) is a combined effect of the CFSST and the bolts, which are connected in series. The predicted initial stiffness of the CFSST with bolts can be determined as:

$$K_{i,p} = \frac{1}{\frac{1}{K_{i,p}^{CFSST}} + \frac{1}{2K_i^{bolt}}} \quad (4)$$

where $K_{i,p}^{CFSST}$ is predicted by Eq. (3) and K_i^{bolt} is the initial stiffness of a single bolt (type D) that is measured as 52.4 kN/mm (Li and Zhao [36]). The predicted and experimental initial stiffness of CFSSTs under tension ($K_{i,p}$ and $K_{i,t}$, respectively) is plotted in Fig. 27, which shows an acceptable agreement. The average ratio of $K_{i,p}$-to-$K_{i,t}$ is 1.08 and the coefficient of variation (COV) is 0.17.

6.1.2 Yield capacity

Owing to symmetric, flexible part of the beam can be modeled as a beam in Fig. 26 (c) with one end as fixed and the other end as roller supported. The bending moment diagram could then be obtained and the maximum bending moment at F can be determined by Eq. (5):

$$M = \frac{1}{2} F \frac{b_{tube} - t_{tube} - W}{2} \quad (5)$$

where b_{tube} is width of tube, t_{tube} is thickness of tube, W is bolt distance.

At yielding state, complete yielding is assumed in tube face walls. The yield moment can be determined in Eqs. (6-7):

$$M_y = \frac{f_y l_{eff} t_{tube}^2}{4} \quad (6)$$

$$l_{eff} = l_{tube} \quad (7)$$

where f_y is 0.2% proof stress of stainless steel, l_{eff} is effective length of CFSST which is adopted as tube length (l_{tube}) in this study. As the resistance is equal to the action (i.e., $M = M_y$), the applied force

(F) could be calculated and the yield capacity ($N_{y,p}$) of CFSST is two times of F. Therefore, $N_{y,p}$ of CFSSTs is calculated by Eq. (8):

$$N_{y,p} = \frac{8M_y}{(b_{tube} - t_{tube} - W)} \tag{8}$$

where M_y is determined in Eq. (6). A comparison of the experimental and predicted yield capacities of CFSSTs is plotted in Fig. 27 (in red color). The averaged predicted-to-experimental ratio of yield capacities is 1.03 and the coefficient of variation is 0.16. In general, the prediction agrees well with the experimental results.

6.1.3 Load-displacement model

Based on experimental and numerical results, the load-displacement (N-Δ) relationship could be illustrated as shown in Fig. 28, which consists of an initial elastic part, a nonlinear transition part and a linearly strain hardening part. By analyzing the shape of N-Δ curve, Eq. (9) is proposed to model the N-Δ relationship of CFSSTs, which consists of an exponential first portion and a straight-line second portion.

$$N = N_o[1 - \exp(-\frac{\Delta}{2})] + K_2\Delta \tag{9}$$

where N_o is the intercept of the load axis by the linear second portion that is named as nominal load in this study and K_2 is the slope of the linear second portion.

As shown in Fig. 28, the yield capacity (N_y) is generally lower than N_o. By evaluating N_y and N_o of FE specimens, the nominal load (N_o) mainly controlled by the yield capacity (N_y), layout of bolts (W and L) and tube size (i.e., tube width, b_{tube}). A total of 10 FE specimens were adopted for regression analysis and their details are given in Fig. 29. The material properties of these FE specimens were same as those of tested specimens. An empirical formula is proposed for the calculation of N_o:

$$N_o = N_y(1+1.2\frac{W}{b_{tube}}+0.6\frac{L}{b_{tube}}) \quad (10)$$

After the determination of N_o, K_2 can be calculated by Eq. (11) as the FE value if knowing the N-Δ curve.

$$K_2 = \frac{N_{30}-N_o}{\Delta_{30}} \quad (11)$$

where Δ_{30} and N_{30} is the displacement of 30 mm and its corresponding load that can be read from the N-Δ curve. Point (Δ_{30}, N_{30}) is located in the strain hardening portion of the N-Δ curve and it is arbitrarily selected for the definition of K_2. The selected displacement of 30 mm is quite large, i.e. about 20% of the tube width.

Based on experimental observations and FE results, the strain hardening feature of the N-Δ curve for CFSSTs is caused by the membrane effect of tube face wall at large deformation and the strain hardening of stainless steel material. At large deformation (e.g., Δ_{30}=30 mm), plastic hinges are formed at both the tube corners and the lines where bolts are located (see failure modes of CFSSTs and Fig. 26). This study assumes that K_2 is related to the width of tube (b_{tube}), yield stress of tube (i.e., 0.2% proof stress, f_y) and the layout of bolt (W). By regressing the FE value of K_2 defined in Eq. (11) (as shown in Fig. 29 with R^2=0.80), Eq. (12) is proposed to predict K_2.

$$K_2 = 2.87\ln(\frac{t_{tube}}{\sqrt{f_y}}W)-1.98 \quad (12)$$

where K_2 is in kN/mm, t_{tube} and W are in mm, and f_y is in MPa. Therefore, N-Δ curves of CFSSTs can be obtained by Eqs. (9, 10 and 12). After knowing N-Δ curves, the ultimate capacity can be directly extracted from the curves as Δ_u has been predefined in Section 3.1.

The proposed load-displacement model is verified by the experimental and FE curves as shown in Fig. 30. It is necessary to mention that the experimental specimens and FE specimens in Fig. 30 were

not used for the regression analysis in deriving the load-displacement model. In general, the predicted curves match well with the experimental and FE curves except few specimens. For specimen F-t3-100x50-M16D and F-t3-100x100-M16D, the prediction is higher than the experimental curves when approaching the failure load. This is caused by the severe plasticization and stress concentration around bolt holes due to the relatively small thickness of tube. For specimen F-t9-75x75-M16D, similar deviation occurs and it is owing to the completed yielding of bolts which cannot sustain the applied load increasingly. These prediction errors are reasonable since the proposed model is only valid for CFSSTs and cannot account for the effects of bolts (e.g., rupture, complete yielding and punching shear failure). It is necessary to mention that the peak load in Fig. 30 is unlikely to be reached in a connection due to the extensive deformation of CFSSTs. A comparison between the predicted ultimate capacity ($N_{u,p}$) and experimental ultimate capacity ($N_{u,t}$) is shown in Fig. 27 and the average of $N_{u,p}/N_{u,t}$ ratios is 1.10 with coefficient of variation (COV) of 0.19. If excluding the data of specimen F-t3-50x100-M16D that seems unreliable, the average of $N_{u,p}/N_{u,t}$ and COV are reduced to 1.02 and 0.12. Therefore, the proposed model is accurate and reliable to predict the load-displacement response of CFSSTs.

6.2 T-to-CFSST

6.2.1 Initial stiffness

A T-to-CFSST connection consists of a CFSST, two T-stubs and bolts, which are connected in series. For assessing the initial stiffness, each component is regarded as a spring. Fig. 31 shows the sketch of T-to-CFSST connection and the layout of springs (i.e., components). Based on component method [30, 51], the initial stiffness of the system ($K_{i,t}^{\text{T-to-CFSST}}$) could be predicted as:

$$K_{i,t}^{\text{T-to-CFSST}} = \frac{1}{\frac{1}{K_i^{\text{CFSST}}} + \frac{2}{K_i^{\text{T}}} + \frac{1}{2K_i^{\text{bolt}}}} \tag{13}$$

where $K_{\mathrm{i}}^{\mathrm{CFSST}}$ is the initial stiffness of CFSST, which could be determined by Eq. (3), $K_{\mathrm{i}}^{\mathrm{T}}$ is the initial stiffness of T-stub and $K_{\mathrm{i}}^{\mathrm{bolt}}$ is the initial stiffness of a single bolt.

As the prediction of the initial stiffness of T-stub is beyond the scope of this paper, the experimental value of $K_{\mathrm{i}}^{\mathrm{T}}$, that was measured in the authors' previous paper [36], is adopted in this study. $K_{\mathrm{i}}^{\mathrm{T}}$ is taken as 38.0 kN/mm, which has excluded the influence of bolt stiffness in T-stub test. The initial stiffness of bolts is approximately predicted by Eq. (14) by assuming only elongation occurs in bolts:

$$K_{\mathrm{i,p}}^{\mathrm{bolt}} = \frac{EA_{\mathrm{net}}}{L_{\mathrm{clamp}}} \tag{14}$$

where E is Young's modulus of stainless steel (=195 GPa), A_{net} is the net cross-section area of bolt and L_{clamp} is the clamping depth of bolt that is the summation of the thickness of T-stub flange, tube face wall and nut.

Table 4 shows the prediction of the initial stiffness of T-to-CFSST connection ($K_{\mathrm{i,p}}^{\mathrm{T\text{-}to\text{-}CFSST}}$) and a comparison to the experimental results ($K_{\mathrm{i,t}}^{\mathrm{T\text{-}to\text{-}CFSST}}$). The predicted results show some variations (Mean=0.86 and COV=0.32) and the prediction results are generally lower than experimental results. A reason is that the anchorage effect of blind bolts in concrete, which could improve the stiffness, is not considered in the predictions due to the complexity of the configurations of different types of blind bolts. Furthermore, the washer/nut diameter of bolts in T-to-CFSST tests is different from that in T-stub tests, which probably leads to an inaccurate $K_{\mathrm{i,t}}^{\mathrm{T}}$ in Table 4. It is found in Table 4 that the initial stiffness of T-stub is much less than that of CFSSTs and bolts, indicating the initial stiffness is mainly controlled by T-stub for specimens tested in this study. This is in agreement with the experimental observation that the majority of the displacement of T-to-CFSST connection occurred in T-stubs. In order to ensure the initial stiffness of a connection could meet the design requirement

with sufficient utilization of materials, the initial stiffness of each component is suggested to be comparable.

In order to improve the prediction accuracy for the initial stiffness, coefficients are introduced to approximately consider the effect of anchorage of blind bolts on $K_{i,t}^{CFSST}$ and the effect of washer/nut diameter on $K_{i,t}^{T}$. After refinement, the average ratio is 0.99 with COV of 0.07. Details of deriving these coefficients could be found in Appendix A.

6.2.2 Yield capacity and ultimate capacity

Based on the marked $N_{y,t}$ and $N_{u,t}$ for T-stub, CFSST and T-to-CFSST shown in Figure 32, the minimum capacity of T-stub and CFSST can be approximately adopted as the capacity of T-to-CFSST. This is true for both yield and ultimate capacities. The predicted yield and ultimate capacities for each component are presented in Table 5. In general, the yield capacity of bolt is much higher. It should be noted that the failure mode of CFSST in specimen F-t3-T6-100x100-M12E and F-t6-T6-100x100-M16E (with through rods) is different from that of other specimens.

For T-to-CFSST connections with tube thickness of 6 mm, the capacity of T-Stub is lower than that of CFSST. T-to-CFSST can reach the predicted capacity of T-stub with a slightly larger deformation limit. For 3 mm thick tube, the capacity of CFSST is lower than that of T-stub. T-to-CFSST can reach the predicted capacity of CFSST with a slightly larger deformation limit.

7. Conclusions

Tensile test was conducted for concrete-filled stainless steel tubes (CFSSTs) and stainless steel blind-bolted T-to-CFSST connections. Based on the experimental and theoretical analysis, the following conclusions can be drawn.

(1) Concrete infill could substantially improve the initial stiffness and load-carrying capacity of CFSSTs by resisting the inward deformation of tube side walls and achieving a fixed boundary condition of tube face walls.

(2) Setting anchors in bolts could further enhance the initial stiffness of CFSSTs, since the concrete infill shares part of the load. Anchorage failure occurs much earlier than the punching shear failure of bolts and the deformation of tube face walls is still insignificant.

(3) Due to the different interlocking mechanisms of blind bolts, the structural behavior of T-to-CFSST connections varies for different types of blind bolts. Fracture failure of blind bolts were observed during the experiment for T-to-CFSST connections, indicating that the strength of blind bolt is fully utilized.

(4) In T-to-CFSST connections with through bolts, most of the applied load is directly transferred within the through bolts, resulting in a small deformation and small stress in the tube.

(5) The developed FE model could accurately simulate the structural behavior of CFSSTs and T-to-CFSST connections. Material type, tube length, T-stub thickness, bolt size and bolt layout have significant influences on their structural behavior.

(6) Based on theoretical analysis, formulas proposed in this study could reasonably predict the yield capacity, ultimate capacity, initial stiffness and load-displacement relationship of CFSSTs, and the initial stiffness of T-to-CFSST connections. The yield capacity and ultimate capacity of T-to-CFSST connections are suggested to be taken as the minimum capacities of their components (i.e., CFSST, T-stub and bolt). Due to the lack of experimental data from other researchers, the proposed method is only verified by the data collected in the current study.

Acknowledgements

Research funding provided by Australian Research Council (ARC Discovery Grant DP160100739) is greatly appreciated by the authors. Thanks are due to the technicians in Heavy Structure Laboratory at UNSW, including Dr. Zhen-Tian Chang, Dr. Tuan Le, Mr. Ronald Moncay and Mr. Sanjeewa Herath. The authors appreciate the permission from the Randwick Council to obtain the seawater and sea sand from the Malabar beach. The authors wish to acknowledge CBW Engineering Pty Ltd for providing the stainless steel Lindapter Hollo bolts.

References

[1] T. Barnett, W. Tizani, D. Nethercot, The practice of blind bolting connections to structural hollow sections: A review, Steel & Composite Structures 1(1) (2001) 1-16.
[2] Lindapter HolloBolt. http://www.lindapter.com/Products/Hollo-Bolt_And_Lindibolt/2. (Accessed 23/12/2020.
[3] Flowdrill. https://www.flowdrill.com/usa_en/. (Accessed 23/12/2020.
[4] Ajax Oneside Fastening Stystem B-N012 Innovation data sheet, 1998.
[5] R. Feng, B. Young, Tests of concrete-filled stainless steel tubular T-joints, Journal of Constructional Steel Research 64(11) (2008) 1283-1293.
[6] Blind Bolt, 2020. https://www.blindbolt.co.uk/. (Accessed 23/12/2020.
[7] J. Lee, H. Goldsworthy, E. Gad, Blind bolted T-stub connections to unfilled hollow section columns in low rise structures, Journal of Constructional Steel Research 66(8-9) (2010) 981-992.
[8] J.E. France, J.B. Davison, P.A. Kirby, Moment-capacity and rotational stiffness of endplate connections to concrete-filled tubular columns with flowdrilled connectors, Journal of Constructional Steel Research 50(1) (1999) 35-48.
[9] S. Mourad, Behaviour of blind bolted moment connections for square HSS columns, McMaster University, 1993.
[10] Y.L. Li, J.G. Teng, X.L. Zhao, R.K. Singh Raman, Theoretical model for seawater and sea sand concrete-filled circular FRP tubular stub columns under axial compression, Engineering Structures 160 (2018) 71-84.
[11] M. Bazli, X.-L. Zhao, Y. Bai, R.S. Raman, S. Al-Saadi, Bond-slip behaviour between FRP tubes and seawater sea sand concrete, Engineering Structures 197 (2019) 109421.
[12] Z.-B. Wang, Z. Tao, D.-S. Li, L.-H. Han, Cyclic behaviour of novel blind bolted joints with different stiffening elements, Thin-Walled Structures 101 (2016) 157-168.
[13] J. Wang, L. Chen, Experimental investigation of extended end plate joints to concrete-filled steel tubular columns, Journal of Constructional Steel Research 79 (2012) 56-70.
[14] J. Wang, H. Zhang, Z. Jiang, Seismic behavior of blind bolted end plate composite joints to CFTST columns, Thin-Walled Structures 108 (2016) 256-269.
[15] J.-F. Wang, L.-H. Han, B. Uy, Behaviour of flush end plate joints to concrete-filled steel tubular columns, Journal of Constructional Steel Research 65(4) (2009) 925-939.
[16] L. Guo, J. Wang, S. Wu, L. Zhong, Experimental investigation and analytical modelling of blind bolted flush or extended end plate connections to circular CFDST columns, Engineering Structures 192 (2019) 233-253.

[17] H. Agheshlui, H. Goldsworthy, E. Gad, O. Mirza, Anchored blind bolted composite connection to a concrete filled steel tubular column, Steel and Composite Structures 23(1) (2017) 115-130.
[18] Z. Tao, M.K. Hassan, T.-Y. Song, L.-H. Han, Experimental study on blind bolted connections to concrete-filled stainless steel columns, Journal of Constructional Steel Research 128 (2017) 825-838.
[19] A. Gardner, H. Goldsworthy, Experimental investigation of the stiffness of critical components in a moment-resisting composite connection, Journal of Constructional Steel Research 61(5) (2005) 709-726.
[20] T. Pitrakkos, The tensile stiffness of a novel anchored blind-bolt component for moment-resisting connections to concrete-filled hollow sections, University of Nottingham, 2012.
[21] H. Agheshlui, H. Goldsworthy, E. Gad, S. Fernando, Tensile behaviour of anchored blind bolts in concrete filled square hollow sections, Materials and structures 49(4) (2016) 1511-1525.
[22] T. Pitrakkos, W. Tizani, Experimental behaviour of a novel anchored blind-bolt in tension, Engineering Structures 49 (2013) 905-919.
[23] H. Agheshlui, H. Goldsworthy, E. Gad, H. Yao, Tensile behavior of groups of anchored blind bolts within concrete-filled steel square hollow sections, Journal of Structural Engineering 142(2) (2016) 04015125.
[24] W. Tizani, T. Pitrakkos, Performance of T-stub to CFT joints using blind bolts with headed anchors, Journal of Structural Engineering 141(10) (2015) 04015001.
[25] A. Elamin, W. Tizani, M. Mahmood, Bolts gauge effect on the face bending behaviour of concrete-filled hollow section for hollo-bolted connections, Applied mechanics and materials, Trans Tech Publ, 2015, pp. 105-109.
[26] M. Mahmood, W. Tizani, C. Sansour, Effect of tube thickness on the face bending for blind-bolted connection to concrete filled tubular structures, International Journal of Civil, Architectural, Structural and Construction Engineering 8(9) (2014) 897-903.
[27] H. Yao, H. Goldsworthy, E. Gad, Experimental and numerical investigation of the tensile behavior of blind-bolted T-stub connections to concrete-filled circular columns, Journal of structural engineering 134(2) (2008) 198-208.
[28] S. De Nardin, A. El Debs, An experimental study of connections between I-beams and concrete filled steel tubular columns, Steel and Composite Structures 4(4) (2004) 303.
[29] H. Van-Long, J. Jean-Pierre, D. Jean-François, Extended end-plate to concrete-filled rectangular column joint using long bolts, Journal of Constructional Steel Research 113 (2015) 156-168.
[30] EN1993-1-8, Eurocode 3: Design of steel structures - Part 1-8: Design of joints, 2010.
[31] Y. Kurobane, J.A. Packer, J. Wardenier, N. Yeomans, Design guide for structural hollow section column connections, Verlag TUV Rheinland, 2004.
[32] L. Silva, L. Neves, F. Gomes, Rotational stiffness of rectangular hollow sections composite joints, Journal of Structural Engineering 129(4) (2003) 487-494.
[33] A.M.E.A. Elamin, The face bending behaviour of blind-bolted connections to concrete-filled hollow sections, University of Nottingham, 2014.
[34] H.-T. Thai, B. Uy, Rotational stiffness and moment resistance of bolted endplate joints with hollow or CFST columns, Journal of Constructional Steel Research 126 (2016) 139-152.
[35] Y.L. Li, X.L. Zhao, R.K. Raman Singh , S. Al-Saadi, Experimental study on seawater and sea sand concrete filled GFRP and stainless steel tubular stub columns, Thin-Walled Struct. 106 (2016) 390-406.
[36] Y.-L. Li, X.-L. Zhao, Experimental study on stainless steel blind bolted T-stub to square hollow section connections, Thin-Walled Struct. (2021), accepted for publication
[37] N. Kosteski, J. Packer, Welded tee-to-HSS connections, Journal of Structural Engineering 129(2) (2003) 151-159.
[38] L. Lu, G. De Winkel, Y. Yu, J. Wardenier, Deformation limit for the ultimate strength of hollow section joints, 6th International Symposium on Tubular Structures, Melbourne, 1994, pp. 341-347.
[39] J.A. Yura, N.A. Zettlemoyer, I.F. Edwards, Ultimate capacity equations for tubular joints, Offshore Technology Conference, Offshore Technology Conference, 1980.
[40] X.-L. Zhao, Deformation limit and ultimate strength of welded T-joints in cold-formed RHS sections, Journal of Constructional Steel Research 53(2) (2000) 149-165.
[41] SIMULIA, ABAQUS, 2016.
[42] SIMULIA, Abaqus user's manual, 2016.
[43] X.-Q. Wang, Z. Tao, T.-Y. Song, L.-H. Han, Stress–strain model of austenitic stainless steel after exposure to elevated temperatures, Journal of Constructional Steel Research 99 (2014) 129-139.

[44] Y.-L. Li, X.-L. Zhao, Hybrid double tube sections utilising seawater and sea sand concrete, FRP and stainless steel, Thin-Walled Struct. 149 (2020) 106643.
[45] AS/NZS4673:2001, Cold-formed stainless steel structures, Standards Australia, Sydney, 2001.
[46] J.G. Teng, Y.L. Huang, L. Lam, L.P. Ye, Theoretical model for fiber-reinforced polymer-confined concrete, Journal of Composites for Construction 11(2) (2007) 201-210.
[47] D.J. Carreira, K.-H. Chu, Stress-strain relationship for plain concrete in compression, ACI Journal 82(6) (1985) 797-804.
[48] S. Popovics, A numerical approach to the complete stress-strain curve of concrete, Cement and Concrete Research 3(5) (1973) 583-599.
[49] Z. Tao, Z.-B. Wang, Q. Yu, Finite element modelling of concrete-filled steel stub columns under axial compression, Journal of Constructional Steel Research (89) (2013) 121–131.
[50] L.-H. Han, G.-H. Yao, Z. Tao, Performance of concrete-filled thin-walled steel tubes under pure torsion, Thin-Walled Struct. (45) (2007) 24-36.
[51] S.N. Sadeghi, A. Heidarpour, X.-L. Zhao, R. Al-Mahaidi, A component-based model for innovative prefabricated beam-to-hybrid tubular column connections, Thin-Walled Structures 132 (2018) 265-275.

Appendix A Refined method to predict the initial stiffness of T-to-CFSST connections

A.1 Effect of washer size on the initial stiffness of T-stub

In this study, the initial stiffness of T-stub is adopted as the experimental value from the authors' previous study. The experimental initial stiffness for T-stub is 38.0 kN/mm which has excluded the influence of bolt stiffness.

Because the size of washer or nut in T-to-CFSST test was different from the bolt head size in T-stub test, the T-stub initial stiffness needs to be modified to reflect this influence. It is known that the initial stiffness of a T-stub is proportional to the reciprocal of the cube of m_0 ($1/m_0^3$). A modification factor (k_T) is defined as the ratio of $1/m_0^3$ between T-stub in T-to-CFSST test and T-stub test.

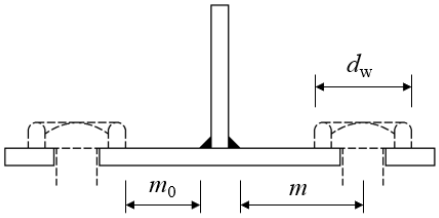

Fig. A.1 T-stub

Table A.1 Modification factor for T-stub.

Specimen	Washer/nut type	d_m (mm)	m_0 (mm)	k_T	$K_{i,T}$ (kN/mm)	$k_T K_{i,T}$ (kN/mm)
Benchmark T test	M16 bolt head	23.8	31.6	N/A	38.0	
F-t3-T6-100x100-M12A	Washer	38.3	24.4	2.19	38.0	83.2
F-t6-T6-100x100-M16A	Washer	38.3	24.4	2.19	38.0	83.2
F-t3-T6-100x100-M12B	M12 Nut-B	24.0	31.5	1.01	38.0	38.5
F-t6-T6-100x100-M16B	M16 Nut	23.8	31.6	1.00	38.0	38.1
F-t6-T6-100x100-M14C	M16 Nut	23.8	31.6	1.00	38.0	38.1
F-t3-T6-100x100-M12D	M12 Nut	18.7	34.2	0.79	38.0	30.2
F-t6-T6-100x100-M16D	M16 Nut	23.8	31.6	1.00	38.0	38.1

Fig. A.2 Washer and nuts used in the experiments.

A.2 Effect of anchorage

As discussed in Section 4.1.2, the initial stiffness of CFSSTs could be greatly enhanced by setting anchors in bolts. The beneficial effect of anchorage on improving the initial stiffness is considered by introducing a coefficient k_{anch}. For blind bolts, the anchorage effect is less significant than that of bolt type E (configuration II) as the interlocking between blind bolt legs and tube face wall is less efficient than nuts. Due to the lack of experimental investigations on the anchorage effect of blind bolts used in this study, k_{anch} is set as 1.5 for blind bolts with regardless of anchorage type which yields the best match between the predicted and experimental initial stiffnesses. If more experimental is available in the future, k_{anch} could be further refined whose value probably depends on the blind bolt type, bolt size and concrete strength.

A.3 Prediction on the initial stiffness of T-to-CFSST connections

By using the modified initial stiffness of T-stub and CFSST, the prediction accuracy for T-to-CFSSTs is greatly improved with average ratio of 0.99 and COV of 0.07.

Table A.3 Predicted initial stiffness of T-to-CFSST connection

Specimen	$K_{i,t}^{T\text{-to-CFSST}}$ (kN/mm)	$K_{i,t}^{T}$ (kN/mm)	$K_{i,p}^{bolt}$ (kN/mm)	$K_{i,p}^{CFSST}$ (kN/mm)	$K_{i,p}^{T\text{-to-CFSST}}$ (kN/mm)	$\frac{K_{i,p}^{T\text{-to-CFSST}}}{K_{i,t}^{T\text{-to-CFSST}}}$
F-t3-T6-100x100-M12A	28.1	83.2	1079.8	79.8	27.0	0.96
F-t6-T6-100x100-M16A	40.1	83.2	1519.9	820.4	39.1	0.97
F-t3-T6-100x100-M12B	16.1	38.4	1071.1	79.8	15.4	0.95
F-t6-T6-100x100-M16B	20.1	38.0	1707.1	820.4	18.5	0.92
F-t6-T6-100x100-M14C	16.2	38.0	1316.1	820.4	18.5	1.14
F-t3-T6-100x100-M12D	11.3	30.2	865.1	53.2	11.7	1.03
F-t6-T6-100x100-M16D	19.1	38.0	1272.3	546.9	18.3	0.96
Mean						0.99
COV						0.07

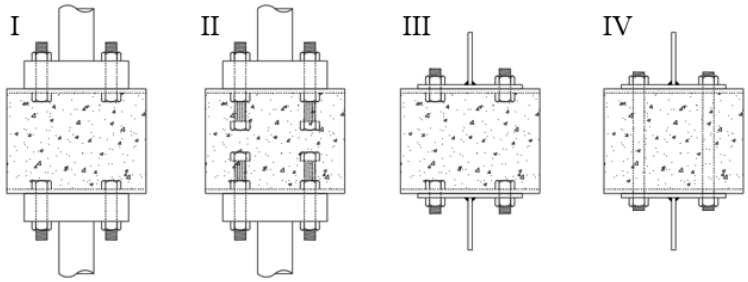

Fig. 1 Specimen configurations.

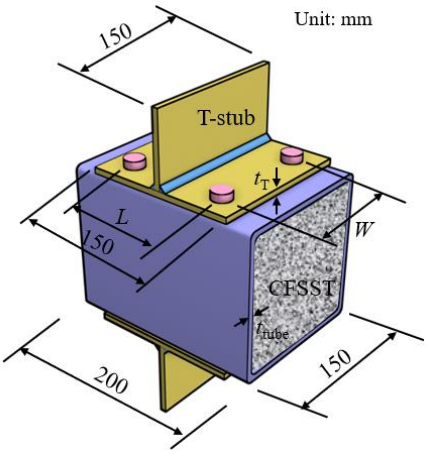

Fig. 2 Dimensions of specimen.

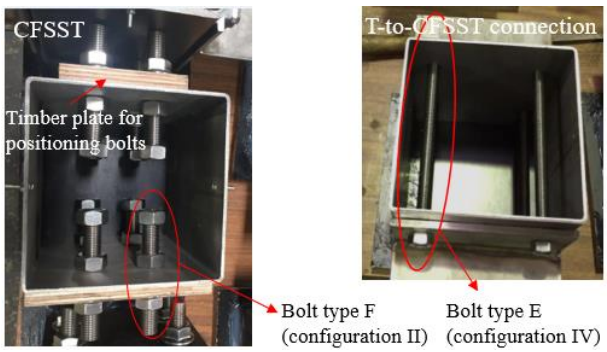

Fig. 3 Specimens before casting concrete.

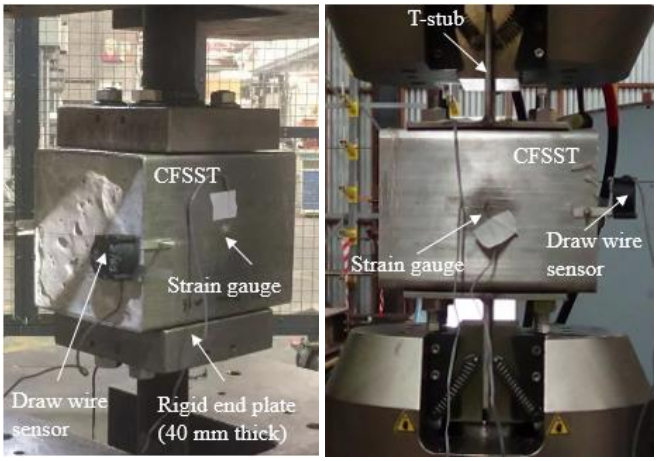

(a) (b)

Fig. 4 Experiment setup: (a) CFSST; (b) T-to-CFSST connection.

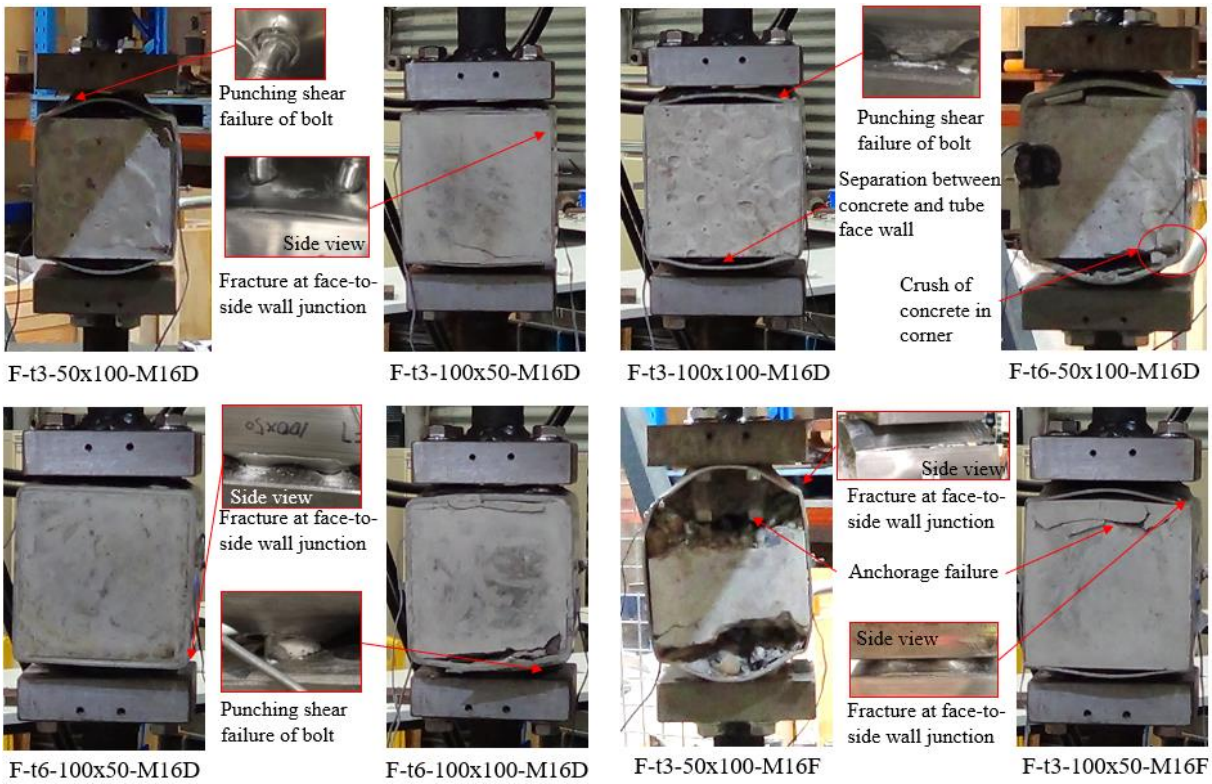

Fig. 5 Failure modes of CFSSTs under tension.

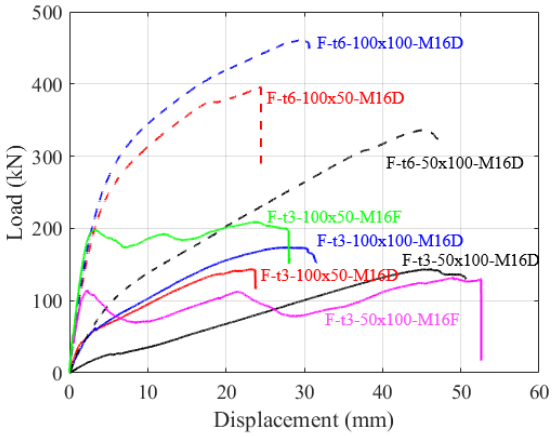

Fig. 6 Load-displacement curves of CFSSTs.

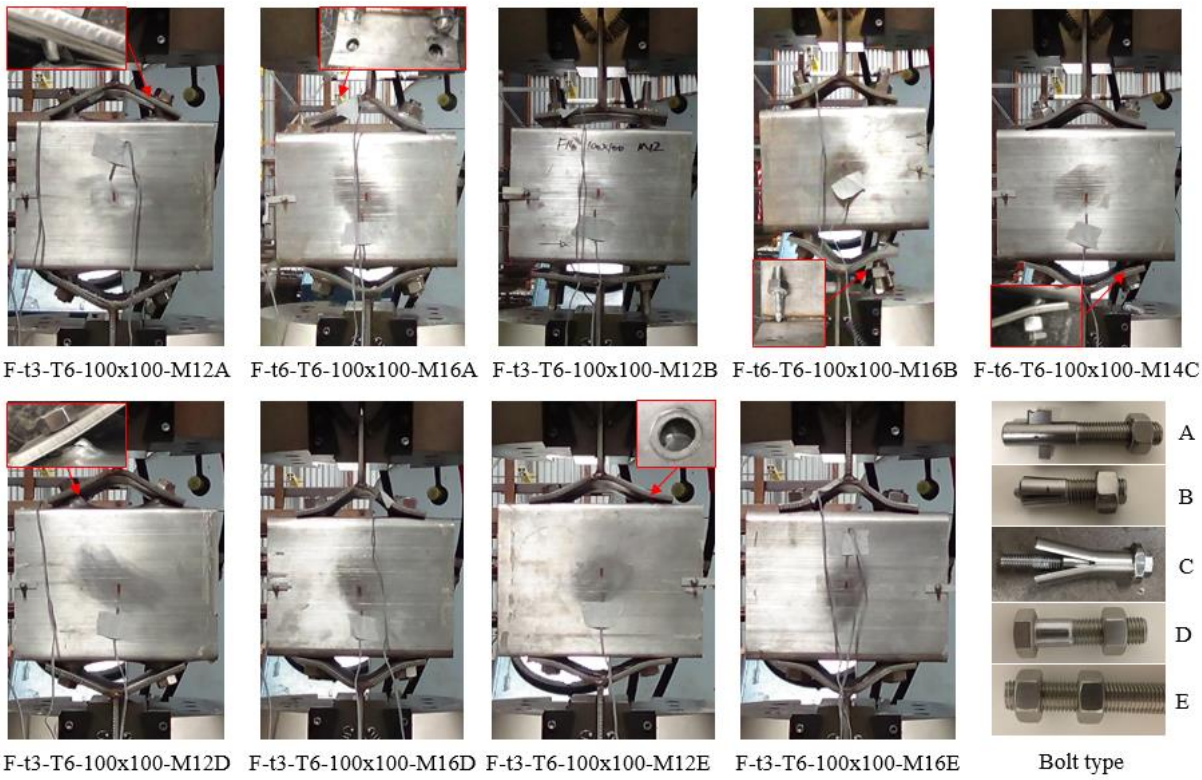

Fig. 7 Failure modes of T-to-CFSST connections.

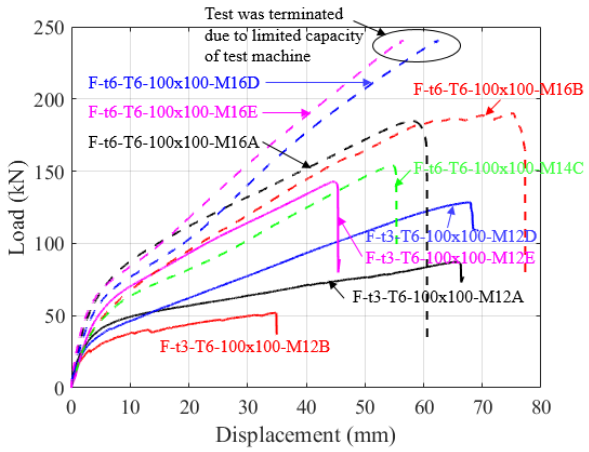

Fig. 8 Load-displacement curves of T-to-CFSST connections.

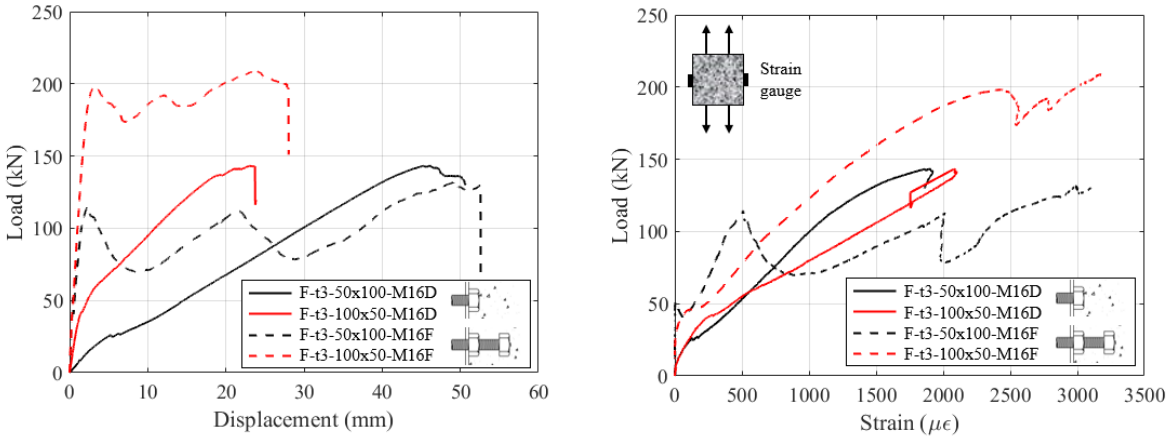

(a) (b)

Fig. 9 Effect of anchorage on the behavior of CFSSTs: (a) load-displacement curves; (b) load-strain curves.

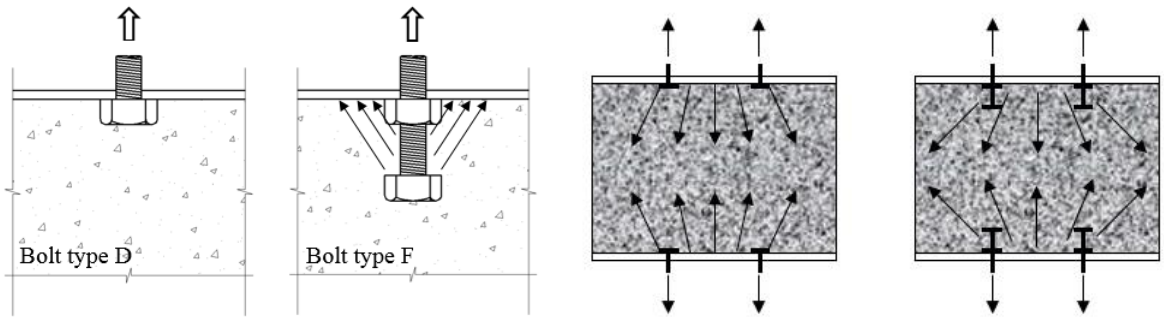

(a) (b)

Fig. 10 Effect of anchorage on stress transfer: (a) tube face wall; (b) concrete and tube side wall.

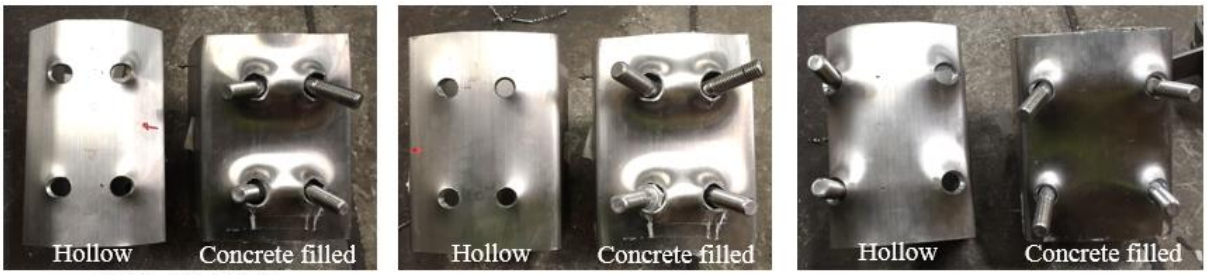

t3-50x100-M16D t6-50x100-M16D t6-100x100-M16D

Fig. 11 Comparison of deformed shapes between CFSSTs and hollow sections.

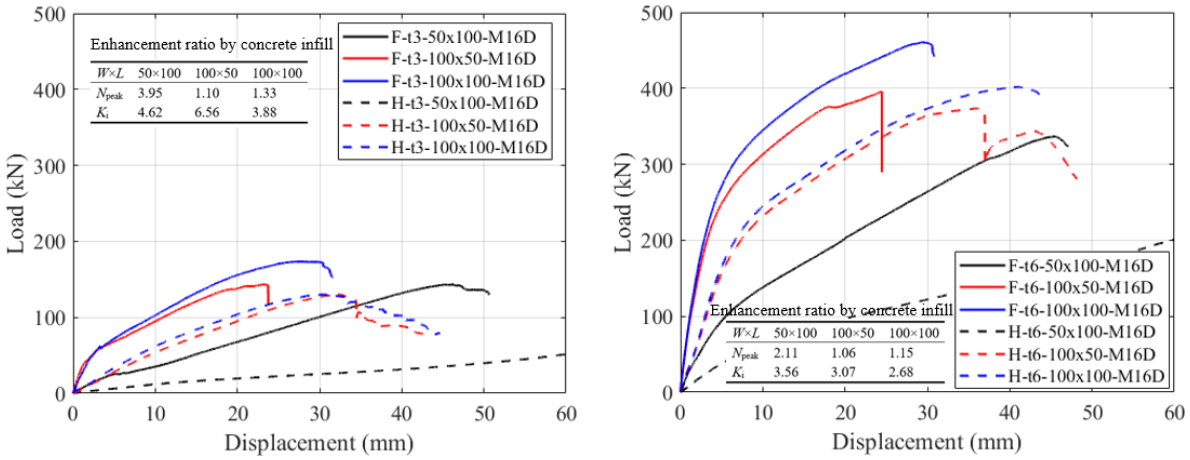

(a) (b)

Fig. 12 Comparison of load-displacement curves between CFSSTs and hollow sections: (a) tube thickness of 3 mm; (b) tube thickness of 6 mm.

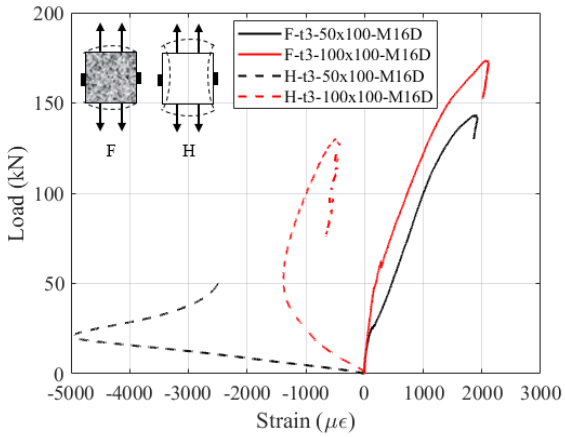

Fig. 13 Comparison of load-strain curves between CFSSTs and hollow sections.

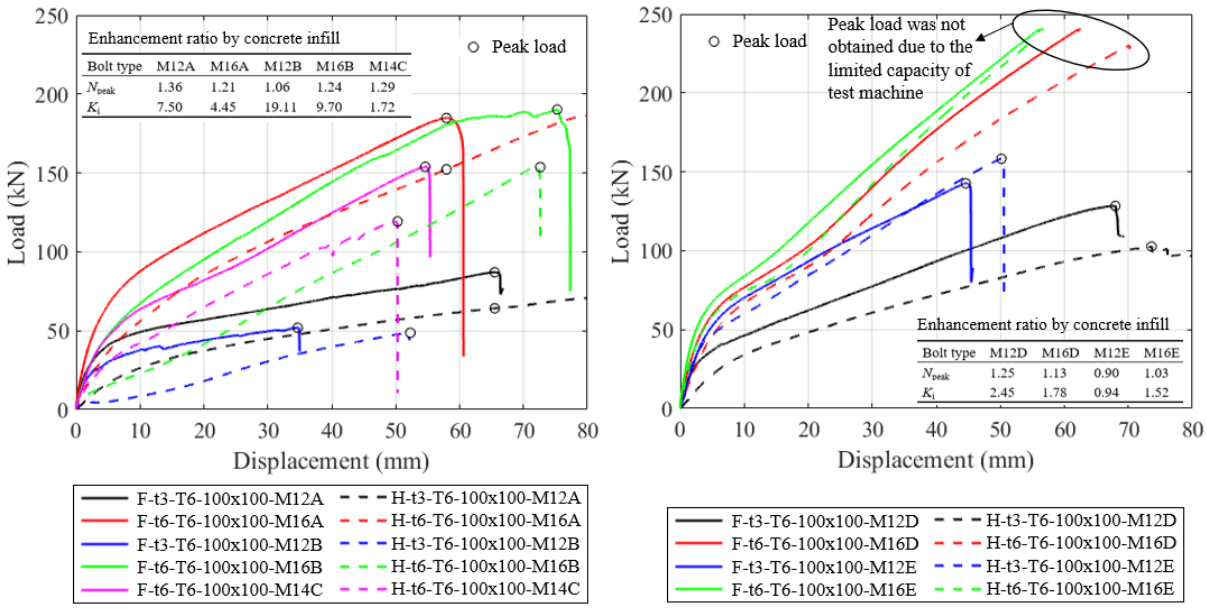

(a) (b)

Fig. 14 Comparison of load-displacement curves between T-to-CFSST and T-to-hollow tube connections: (a) blind bolted; (b) normal bolted.

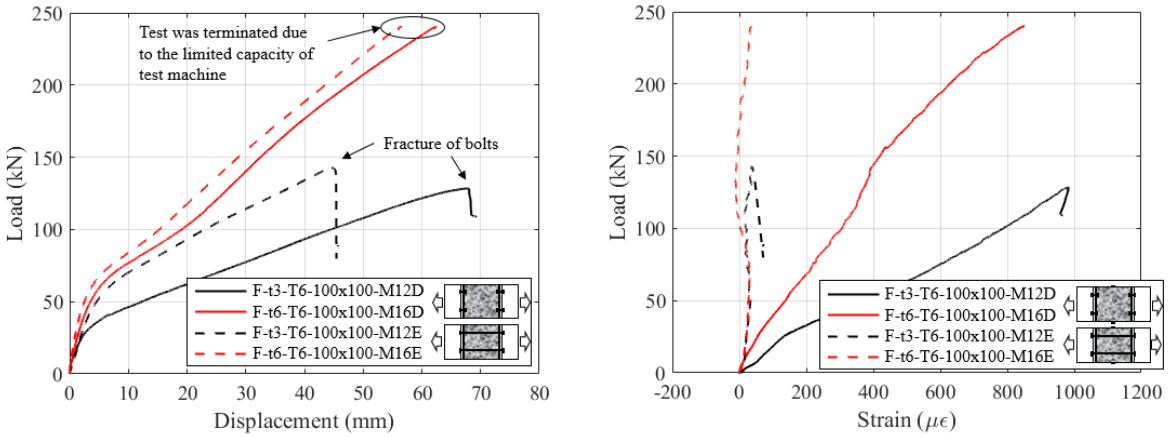

(a) (b)

Fig. 15 Effect of specimen configuration on the behavior of T-to-CFSST connections: (a) load-displacement curves; (b) load-strain curves.

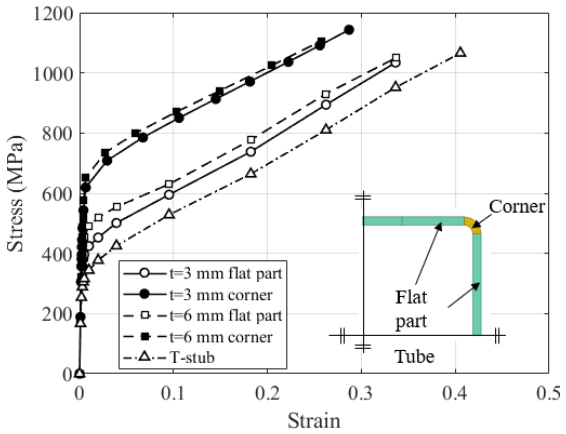

Fig. 16 Stress-strain relationship of stainless stee tube and T-stub for FE model.

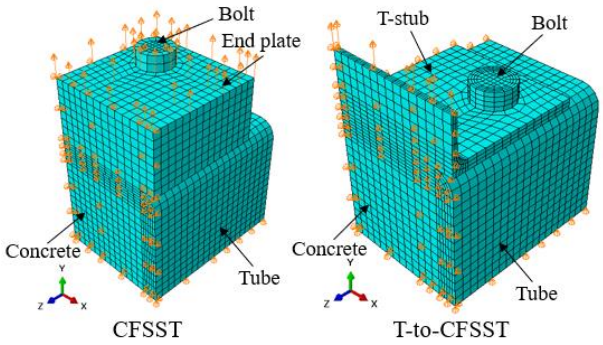

Fig. 17 FE model.

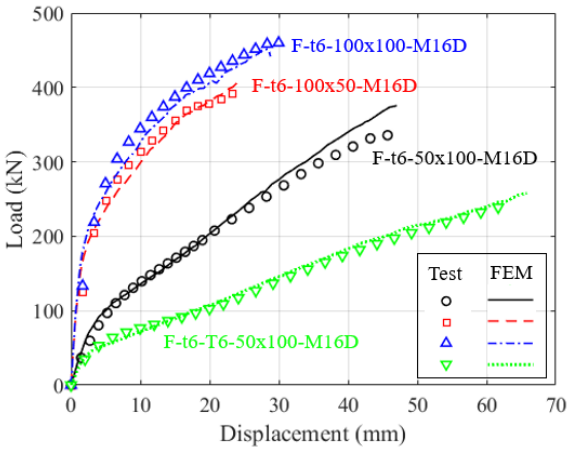

Fig. 18 Verification of load-displacement curves.

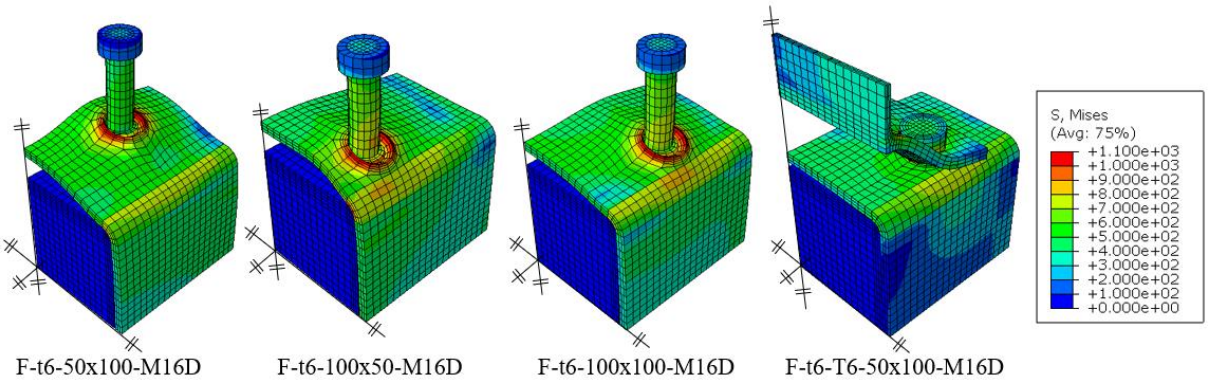

Fig. 19 Failure modes and Mises stress contour of typical specimens (unit: MPa).

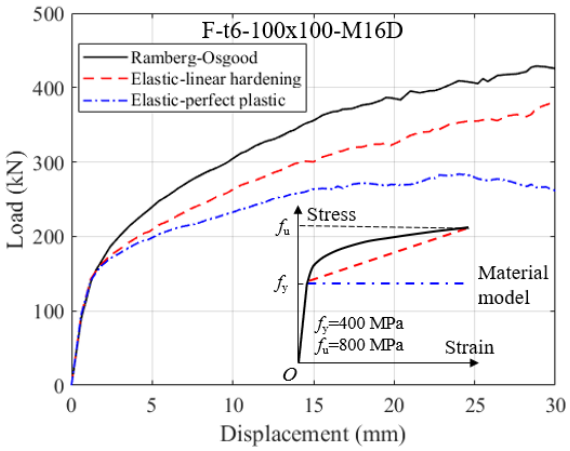

Fig. 20 Effect of material type on load-displacement curves.

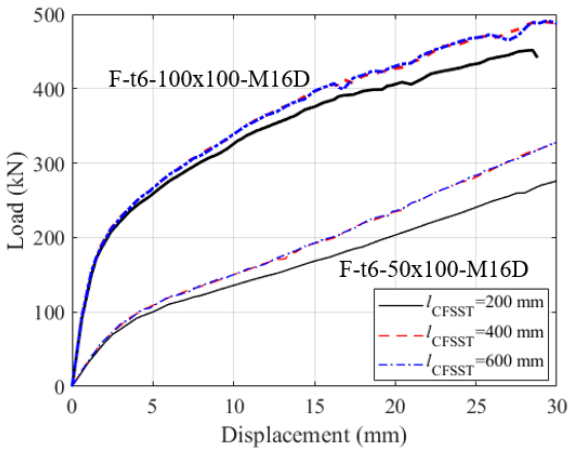

Fig. 21 Effect of CFSST length on load-displacement curves.

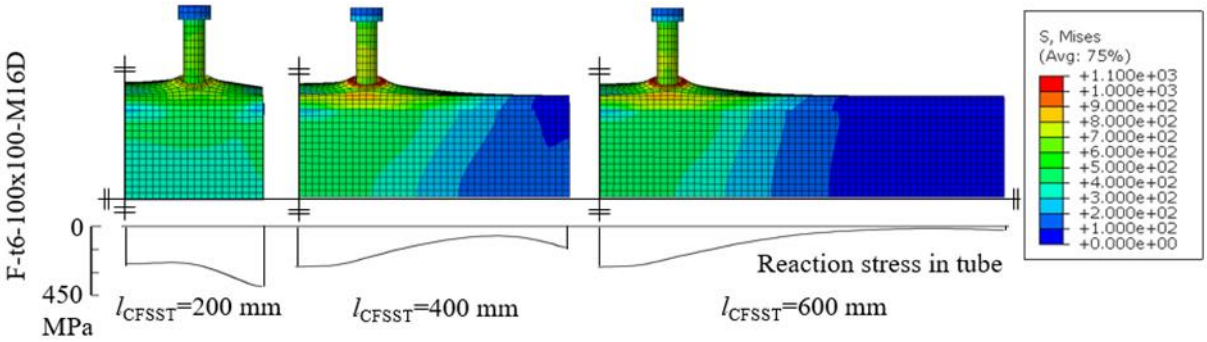

(a)

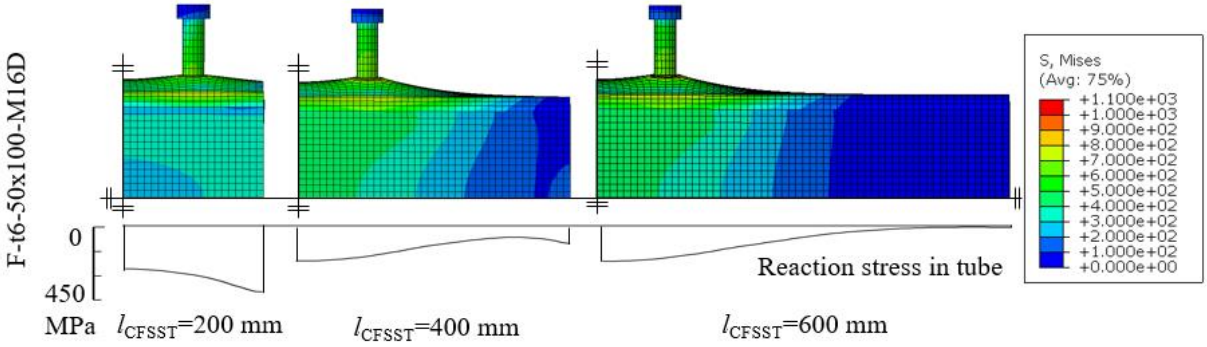

(b)

Fig. 22 Effect of CFSST length on deformed shape and stresses in tube (unit: MPa): (a) F-t6-100x100-M16D; (b) F-t6-50x100-M16D.

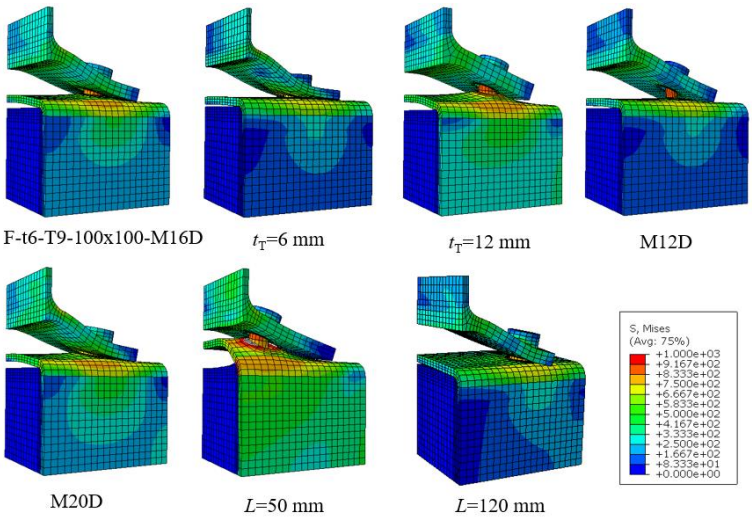

Fig. 23 Deformed shape and Mises stress contour (unit: MPa).

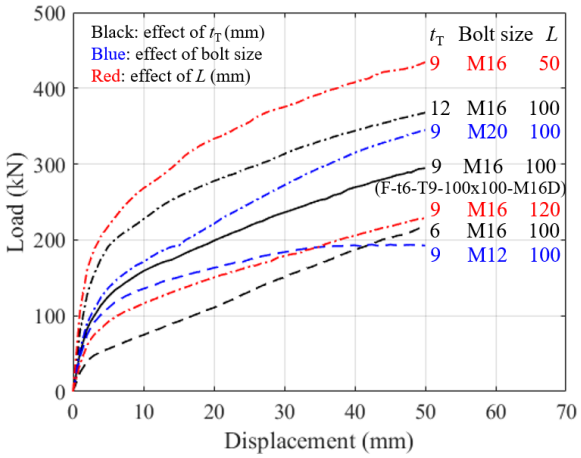

Fig. 24 Effects of T-stub thickness, bolt size and bolt layout on load-displacement curves.

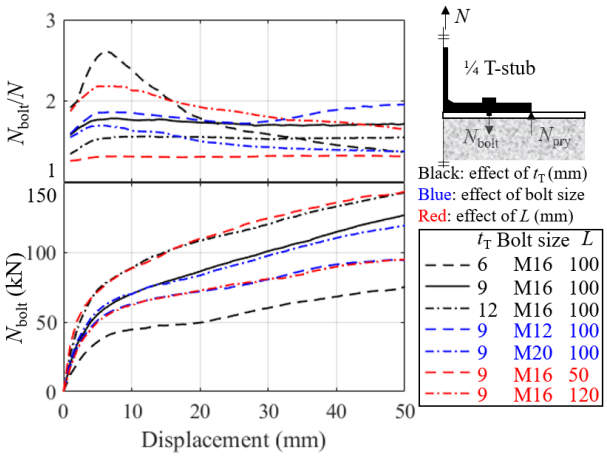

Fig. 25 Effect of T-stub thickness, bolt size and bolt layout on loads in bolt.

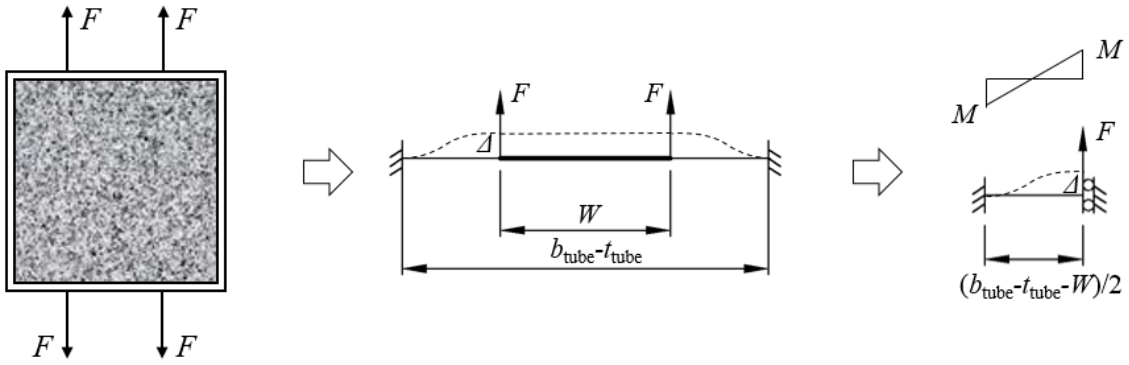

(a) (b) (c)

Fig. 26 Model for initial stiffness and yield capacity prediction: (a) 2-D illustration; (b) face wall model; (c) bending moment diagram.

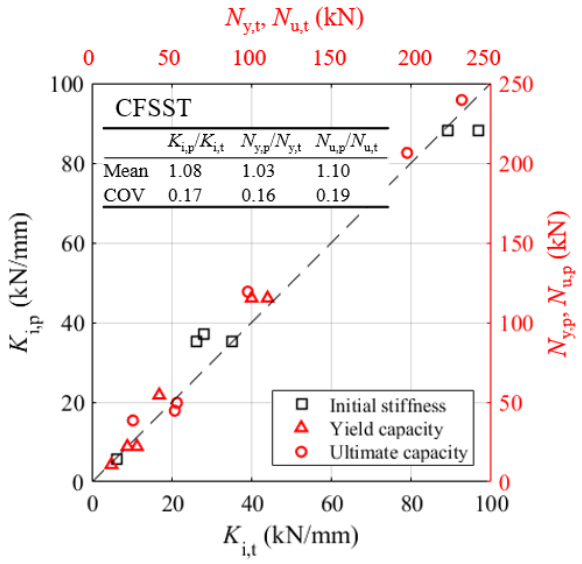

Fig. 27 Prediction of initial stiffness of CFSSTs.

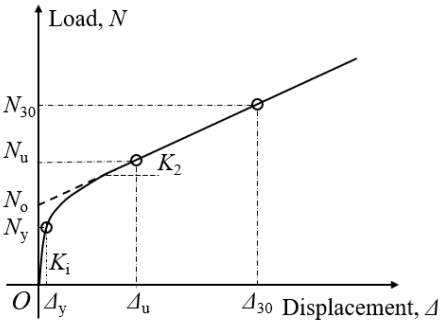

Fig. 28 Theoretical model for load-displacement relationship of CFSSTs.

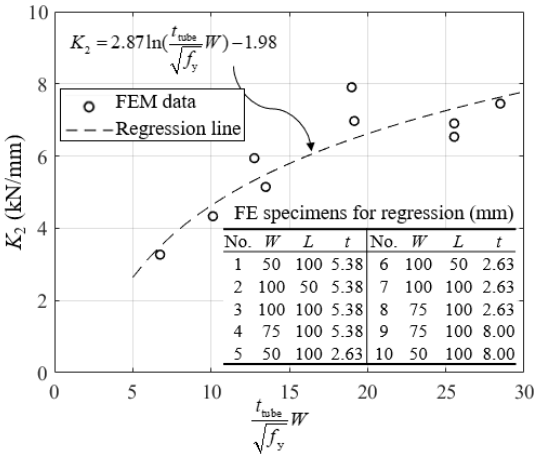

Fig. 29 Determination of K_2.

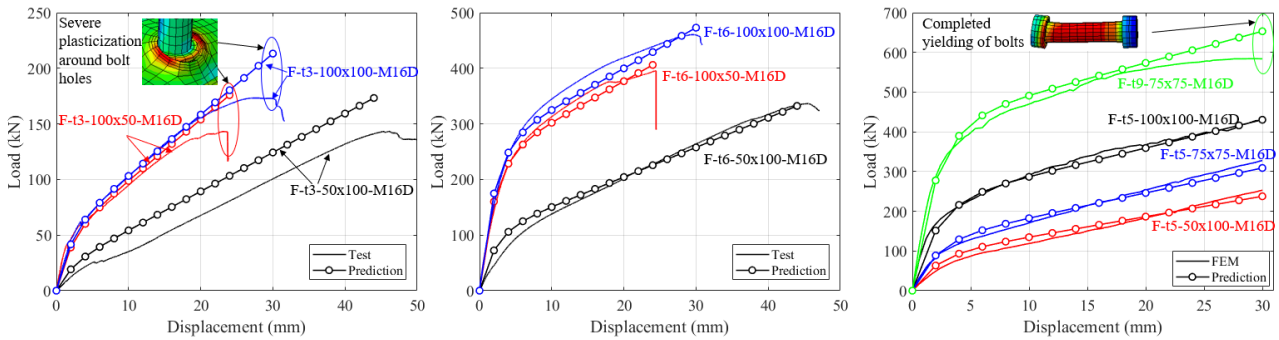

(a) (b) (c)

Fig. 30 Verification of load-displacement model for CFSSTs: (a) experimental specimens with 3 mm thick tube; (b) experimental specimens with 6 mm thick tube; (c) FE specimens.

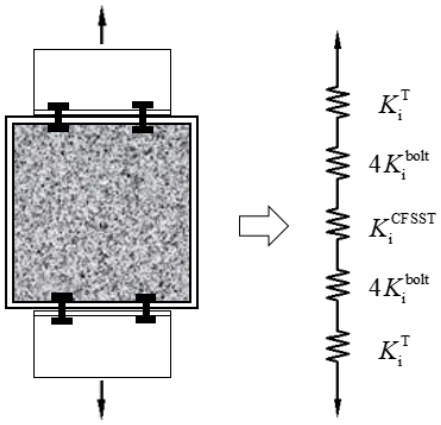

Fig. 31 Component method for the prediction of initial stiffness of T-to-CFSST connections.

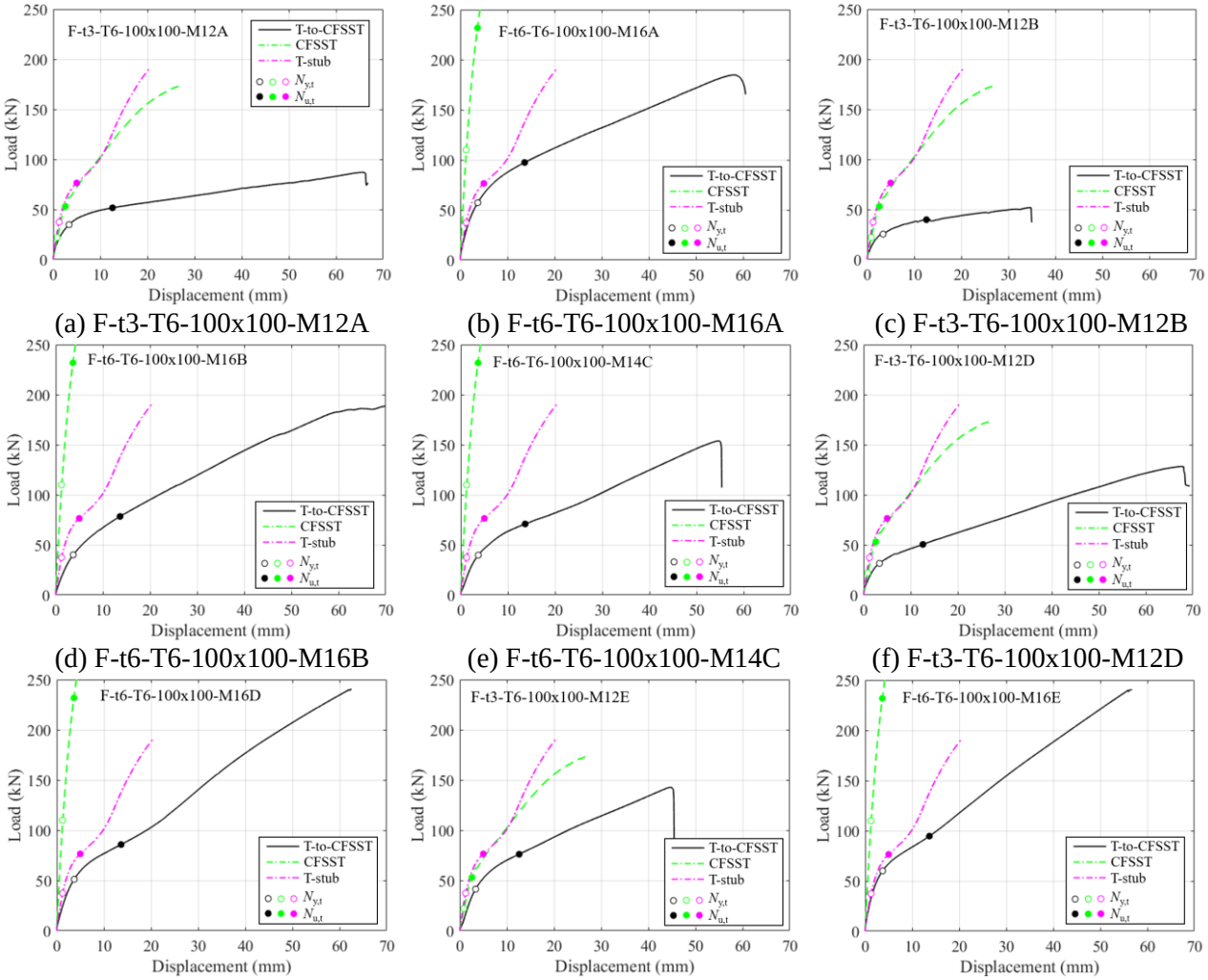

(a) F-t3-T6-100x100-M12A (b) F-t6-T6-100x100-M16A (c) F-t3-T6-100x100-M12B

(d) F-t6-T6-100x100-M16B (e) F-t6-T6-100x100-M14C (f) F-t3-T6-100x100-M12D

(f) F-t6-T6-100x100-M16D (h) F-t3-T6-100x100-M12E (i) F-t6-T6-100x100-M16E

Fig. 32 Comparison of load-displacement curves of T-to-CFSST, CFSST and T-stub.

Table 1 Details of specimens.

Specimen	Layout of bolts		Bolt		Tube	T-stub	Test setup
	W (mm)	L (mm)	Size (mm)	Type	t_{tube} (mm)	t_T (mm)	
F-t3-50x100-M16D	50	50	16	D	2.63	N/A	I
F-t3-100x50-M16D	100	50	16	D	2.63	N/A	
F-t3-100x100-M16D	100	100	16	D	2.63	N/A	
F-t6-50x100-M16D	50	100	16	D	5.38	N/A	
F-t6-100x50-M16D	100	50	16	D	5.38	N/A	
F-t6-100x100-M16D	100	100	16	D	5.38	N/A	
F-t3-T6-50x100-M16F	50	100	16	F	2.63	N/A	II
F-t3-T6-100x50-M16F	100	50	16	F	2.63	N/A	
F-t3-T6-100x100-M12A	100	100	12	A	2.63	5.89	III
F-t6-T6-100x100-M16A	100	100	16	A	5.38	5.89	
F-t3-T6-100x100-M12B	100	100	12	B	2.63	5.89	
F-t6-T6-100x100-M16B	100	100	16	B	5.38	5.89	
F-t6-T6-100x100-M14C	100	100	14	C	5.38	5.89	
F-t3-T6-100x100-M12D	100	100	12	D	2.63	5.89	
F-t6-T6-100x100-M16D	100	100	16	D	5.38	5.89	
F-t3-T6-100x100-M12E	100	100	12	E	2.63	5.89	IV
F-t6-T6-100x100-M16E	100	100	16	E	5.38	5.89	

Table 2 Test results of CFSSTs under tension.

Specimen	$\Delta_{y,t}$ (mm)	$\Delta_{u,t}$ (mm)	$N_{y,t}$ (kN)	$N_{u,t}$ (kN)	$K_{i,t}$ (kN/mm)	Failure mode
F-t3-50x100-M16D	1.93	5.79	12.0	25.5	6.3	Pull out of bolt
F-t3-100x50-M16D	0.82	2.45	28.0	51.7	35.2	Fracture of tube
F-t3-100x100-M16D	0.87	2.60	22.0	53.1	26.0	Pull out of bolt
F-t6-50x100-M16D	1.77	5.32	42.0	97.6	28.1	Pull out of bolt
F-t6-100x50-M16D	1.06	3.17	100.0	197.5	96.9	Fracture of tube
F-t6-100x100-M16D	1.22	3.66	110.0	231.8	89.3	Pull out of bolt
F-t3-50x100-M16F	N/A[a]	2.25	N/A[a]	114.3[b]	120.7	Fracture of tube[c]
F-t3-100x50-M16F	N/A[a]	3.28	N/A[a]	198.2[b]	139.3	Fracture of tube[c]

[a]: Yield capacity cannot be determined from load-displacement curves;
[b]: Load corresponding to the first peak load at anchorage failure;
[c]: Corresponding to the peak load in the whole load-displacement curve.

Table 3 Test results of T-to-CFSST connections.

Specimen	$\Delta_{y,t}$ (mm)	$\Delta_{u,t}$ (mm)	$N_{y,t}$ (kN)	$N_{u,t}$ (kN)	$K_{i,t}$ (kN/mm)	Failure mode
F-t3-T6-100x100-M12A	3.37	12.60	34.8	51.7	28.1	Fracture of bolt
F-t6-T6-100x100-M16A	3.72	13.66	57.3	97.4	40.1	Fracture of bolt
F-t3-T6-100x100-M12B	3.37	12.60	25.4	39.8	16.1	Pull out of bolt
F-t6-T6-100x100-M16B	3.72	13.66	40.1	78.4	20.1	Fracture of bolt
F-t6-T6-100x100-M14C	3.72	13.66	39.8	70.9	16.2	Fracture of bolt
F-t3-T6-100x100-M12D	3.37	12.60	31.6	50.5	11.3	Pull out of bolt
F-t6-T6-100x100-M16D	3.72	13.66	51.2	85.8	19.1	N/A[a]
F-t3-T6-100x100-M12E	3.37	12.60	41.4	76.1	15.0	Fracture of bolt
F-t6-T6-100x100-M16E	3.72	13.66	60.1	94.7	31.8	N/A[a]

Table 4 Prediction of initial stiffness of T-to-CFSST connections.

Specimen	$K_{i,t}^{T\text{-to-CFSST}}$ (kN/mm)	$K_{i,t}^{T}$ (kN/mm)	$K_{i,p}^{bolt}$ (kN/mm)	$K_{i,p}^{CFSST}$ (kN/mm)	$K_{i,p}^{T\text{-to-CFSST}}$ (kN/mm)	$\frac{K_{i,p}^{T\text{-to-CFSST}}}{K_{i,t}^{T\text{-to-CFSST}}}$
F-t3-T6-100x100-M12A	28.1	38.0	1079.8	53.2	13.9	0.49
F-t6-T6-100x100-M16A	40.1	38.0	1519.9	546.9	18.2	0.45
F-t3-T6-100x100-M12B	16.1	38.0	1071.1	53.2	13.9	0.86
F-t6-T6-100x100-M16B	20.1	38.0	1707.1	546.9	18.3	0.91
F-t6-T6-100x100-M14C	16.2	38.0	1316.1	546.9	18.2	1.13
F-t3-T6-100x100-M12D	11.3	38.0	865.1	53.2	13.9	1.23
F-t6-T6-100x100-M16D	19.1	38.0	1272.3	546.9	18.2	0.95
Mean						0.86
COV						0.32

Table 5 Prediction for the yield and ultimate capacity of T-to-CFSST connections.

Specimen	Predicted yield capacity, $N_{y,p}$ (kN)				Predicted ultimate capacity, $N_{u,p}$ (kN)			
	CFSST	T-stub	Bolt	T-to-CFSST	CFSST	T-stub	Bolt[a]	T-to-CFSST
F-t3-T6-100x100-M12A	22.1	35.8	N/A	22.1	49.6	84.2	95.2	49.6
F-t6-T6-100x100-M16A	115.2	35.8	N/A	35.8	239.6	84.2	236.4	84.2
F-t3-T6-100x100-M12B	22.1	35.8	N/A	22.1	49.6	84.2	88.8	49.6
F-t6-T6-100x100-M16B	115.2	35.8	N/A	35.8	239.6	84.2	128.8	84.2
F-t6-T6-100x100-M14C	115.2	35.8	N/A	35.8	239.6	84.2	196.0	84.2
F-t3-T6-100x100-M12D	22.1	35.8	185.0[b]	22.1	49.6	84.2	329.2	49.6
F-t6-T6-100x100-M16D	115.2	35.8	394.4[b]	35.8	239.6	84.2	440.0	84.2
F-t3-T6-100x100-M12E	22.1	35.8	234.9	22.1	49.6	84.2	291.6	49.6
F-t6-T6-100x100-M16E	115.2	35.8	344.2	35.8	239.6	84.2	451.2	84.2

[a]: Tested ultimate capacity from Li and Zhao [36]

[b]: Yield capacity is equal to the tested yield stress multiplied by the net cross-sectional area